Coherent Manipulations of Trapped $^{88}Sr^{+}$ using the $4D_{5/2} \rightarrow 5S_{1/2}$ Transition

by

Ruth Shewmon

Submitted to the Department of Physics
in partial fulfillment of the requirements for the degree of

Bachelor of Science in Physics

at the

MASSACHUSETTS INSTITUTE OF TECHNOLOGY
[June 2008]
May 2008

© Ruth Shewmon, MMVIII. All rights reserved.

The author hereby grants to MIT permission to reproduce and distribute publicly paper and electronic copies of this thesis document in whole or in part.

Author .....
Department of Physics
May 22, 2008

Certified by.....
Isaac Chuang
Associate Professor, Departments of Physics and EECS
Thesis Supervisor

Accepted by .....
David Pritchard
Thesis Coordinator

MASSACHUSETTS INSTITUTE OF TECHNOLOGY
JUN 13 2008
LIBRARIES

ARCHIVES

Coherent Manipulations of Trapped $^{88}Sr^{+}$ using the $4D_{5/2} \rightarrow 5S_{1/2}$ Transition

by

Ruth Shewmon

Submitted to the Department of Physics
on May 22, 2008, in partial fulfillment of the
requirements for the degree of
Bachelor of Science in Physics

Abstract

The ability to control quantum systems with high fidelity is of fundamental importance to a variety of scientific experiments. This thesis describes the frequency stabilization of a laser which is used to coherently manipulate both the internal electronic state and quantum harmonic motion of a trapped $^{88}Sr^{+}$ ion via its $4D_{5/2} \leftrightarrow 5S_{1/2}$ transition. The laser is locked with a linewidth on the order of 1Hz to the resonance of a high-finesse optical cavity. However, acoustic and thermal noise in the cavity broadens the laser's linewidth to several hundreds of Hertz. Despite the noise, we find that the ion's internal electronic state can be manipulated by the laser with a high degree of precision: 17 consecutive Rabi oscillations can be driven with a contrast exceeding 80 percent, and Ramsey inteferometry indicates that phase coherence decays with a time constant of $342 \pm 6 \mu s$. Because the laser's dominant spectral broadening occurs on a slow timescale, phase coherence can be maintained by spin echoes for over 5ms. In addition, laser pulses detuned to the first blue motional sideband are able to control the ion's quantum state of motion well enough to use the ground and first excited states as a second qubit. This allows a two-qubit controlled-NOT gate, the quantum analog of an XOR gate and a fundamental building block of quantum computation, to be demonstrated on a single $^{88}Sr^{+}$ ion with a classical fidelity of 0.89 ± 0.02.

Thesis Supervisor: Isaac Chuang
Title: Associate Professor, Departments of Physics and EECS

Acknowledgments

The work described in this thesis could not have happened without the valuable help and insights provided by a number of wonderful people. I am grateful not only for their assistance in this particular venture, but also because working with them has inspired and enabled me to become a better scientist. First of all, the members of the Quanta research group as a whole have made the past year and a half a great experience both in and outside of lab. From the very beginning of my time with this group, Jaroslaw Labaziewicz has been a fantastic mentor in particular. The depth of his scientific knowledge and his level of expertise in constructing and repairing the machinery of our experiments are truly awe-inspiring. I can't thank him enough for the massive amount of his time that I have taken while he taught me most of the experimental tricks I know. I of course owe an enormous debt to Prof. Isaac Chuang, who has been the guiding force behind this entire research experience. I am consistently amazed at how freely he gives his time to help his students, never hesitating to drop whatever he is doing to provide insightful answers to even the most commonplace questions. He has challenged me at every step of the way to strive for higher standards, which has helped me to accomplish many things I never thought were possible.

Contents

List of Figures

Chapter 1

Introduction

1.1 Context

Ion traps create a nearly ideal environment in which to explore one of Nature's purest and most elegant quantum systems: the atom. Because trapped ions are suspended in free space by electromagnetic fields, they can be extremely well-isolated from interaction with their environment. Laser cooling and spectroscopy techniques used in combination with ion traps have historically provided important tests of the fundamental principles of quantum mechanics[BHI$^+$91, SNBT86, For93].

Today there is a growing emphasis in atomic physics experiments on high-fidelity control over quantum systems, another task for which ion traps are ideally suited. In precision spectroscopy, a properly entangled ensemble of N atoms could reach a quantum limit of resolution that is below the shot noise limit by a factor of $\sqrt{N}$[GLM04]. Quantum information techniques have also enabled the creation of an atomic clock from trapped Al^+ and and Be^+ that has an astounding 17 digits of precision[RHS$^+$08]. Feynman famously noted that many computationally intractable problems in physics could be efficiently simulated by a well-controlled quantum system [Fey82], and idea that was further expanded by Deutsch into the universal quantum computer [Deu85]. Networks of ion traps arranged on the surface of a chip provide a potentially scalable architecture for quantum simulation and computation[CZ95]. In this scheme, each ion holds a qubit in its internal electronic state and information is transferred via the

collective motional modes of several ions in the same trap.

The same sensitivity to phase that makes quantum information so powerful also presents an enormous challenge to experimentalists, who are charged with creating a system that is paradoxically both isolated and controllable. In this thesis, the system of choice is the optical $4D_{5/2} \leftrightarrow 5S_{1/2}$ qubit of a single $^{88}Sr^{+}$ ion. The energy level structure is essentially identical to that of $^{40}Ca^{+}$, which has played an important role in the development of trapped-ion quantum computers[SKHR+03, RLCB+03]. Strontium has the additional advantage that all relevant transitions are addressable by commercially available diode lasers, which require less experimental overhead. The monumental task of building a system to trap the ion in a pristine environment has already been accomplished by the painstaking efforts of previous students. This work focuses on controlling the ion's state while introducing as little additional noise as possible.

1.2 Overview

This thesis can be conceptually divided into three parts. The first contains introductory material. The second shows the construction of a laser frequency stabilization system for the 674nm qubit laser, designed to bring a high level of precision to our control of the strontium ion via the $4D_{5/2} \leftrightarrow 5S_{1/2}$ transition. The third and final portion describes a few of the explorations made possible by this new tool.

In the course of this discussion, I have two main questions in mind. First, what is the longest coherence time that can be achieved while controlling the ion's electronic state? In addition to evaluating the purity of the classical control signals carried by the new laser, we can explore methods of recovering from decoherence that take advantage the unique and counterintuitive properties of quantum information. The second question is, can the quantum motion of the ion be coherently controlled by coupling it to the ion's electronic state? This is difficult because the weakness of this coupling makes for slow interactions that push the boundaries of available coherence time.

Here is a guide to the chapters in this thesis:

Chapter 2 introduces the coherent control of trapped $^{88}Sr^{+}$ ions with lasers. Sections 2.1 and 2.2 describe the interaction of a coherent light source with an atom's electronic and motional states. Section 2.3 is devoted to the decoherence of quantum information: how it arises in our system, and a series of experiments to better understand its nature. Section 2.4 explains the relevant level structure of $^{88}Sr^{+}$.

Chapter 3 begins the discussion of laser stabilization. Section 3.1 is a theoretical description of the Pound-Drever-Hall laser locking technique, which uses a high finesse optical cavity as a frequency reference. In section 3.2, the design of such a frequency stabilization system is presented.

Chapter 4 evaluates the performance of the system designed in chapter 4. Section 4.1 measures the stability and linewidth of the optical cavity frequency reference. Section 4.2 examines the lock's ability to hold the laser to this reference.

Chapter 5 explores the coherence of quantum information stored in the atom's internal state. Section 5.1 shows the increased duration and amplitude of coherent driven oscillations. In section 5.2, Ramsey interferometry and spin echo techniques are used to explore phase coherence. Section 5.3 implements the BB1 algorithm for generating composite pulses that are less sensitive to laser amplitude noise.

Chapter 6 demonstrates quantum control of both the $^{88}Sr^{+}$ ion's internal and motional state, made possible by the increased coherence times associated with the newly stabilized laser. Section 6.1, shows the sideband Rabi oscillations that indicate coherent control of quantum motion. Section 6.2 describes the measurement of single-pulse rotations acting on both qubits. Section 7.3 demonstrates a controlled-NOT operation, a fundamental building block of quantum control.

Chapter 7 concludes with a discussion of the experimental results.

Appendix A describes in more detail how the abstract quantum system of chapter 2 is realized experimentally. Section A.1 explains how ion traps confine $^{88}Sr^{+}$ in oscillating electric fields. Section A.2 presents an overview of the apparatus.

1.3 Contributions to this work

This work was performed in Isaac Chuang's laboratory at the MIT-Harvard Center for Ultracold Atoms. Jaroslaw Labaziewicz and Kenneth Brown led the construction of the apparatus described in chapter 3. Labaziewicz oversaw my work directly, which consisted of the construction, debugging, and final characterization of the laser lock, the design of a vacuum environment and mount for the optical frequency reference cavity, an upgrade to the capabilities of the laser pulse sequencing software, and the design of a series of pulse sequences. Most of the ion trapping was also performed by Labaziewicz, later assisted by Shannon Wang as well as myself. Wang was additionally responsible for building the niobium magnetic field stabilizers. We are all deeply indebted to Yufei Ge, who microfabricated the ion traps used in these experiments.

Financial support for this work was provided by the National Science Foundation, the Japan Science and Technology Foundation, and the MIT Undergraduate Research Opportunity Program.

Chapter 2

Background: Coherent Manipulations of Trapped $^{88}Sr^{+}$

Ion traps are an important tool for atomic physicists because they allow a simple quantum system to be almost completely isolated from decoherence caused by interaction with its environment. Experiments of fundamental importance in precision spectroscopy [WIBH87, BSW82] and tests of quantum mechanical principles [BHI+91, SNBT86, For93] have been performed in ion traps. Trapped ions have also been used to make very stable atomic clocks[MBH+04, DUB+01]. The same properties that make trapped ions so ideal for precision experiments have also motivated their use in the field of quantum computation, where trapped ions have been proposed as the basis for a scalable quantum architecture [CZ95].

Ion traps enable precision experiments not only because they provide isolation, but also because they allow for highly controllable interactions mediated by lasers. In this chapter, I explain how a trapped $^{88}Sr^{+}$ ion's quantum state can be coherently manipulated by resonant pulses of light. Section 2.1 describes the ion as a two-state system suspended in a harmonic potential, and shows how it interacts with a coherent light source. Section 2.2 introduces the theory of coherent operations on abstract qubits, and shows how these concepts can be applied to a trapped ion. Section 2.3 discusses the decoherence of quantum information that makes coherent control so challenging in practice. Included in this discussion are experimental tools for

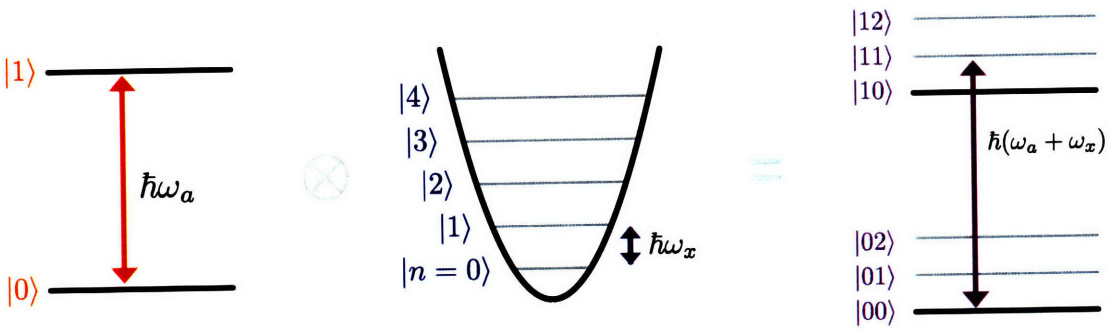

Figure 2-1: The internal (left) atomic energy levels are dressed by the motional states (center) of the ion trapped in a harmonic potential. As shown on the right, a laser beam detuned by $\hbar\omega_x$ addresses a transition between internal and motional states simultaneously.

understanding and mitigating the effects of decoherence, which are used in chapters 5 and 6. Finally, section 2.4 introduces the $^{88}Sr^{+}$ ion, the atomic system in which all of these experiments take place.

2.1 Atom-laser interactions

At the most fundamental level, this thesis is about the interaction of a single-mode coherent light source with a two-level atom trapped in a harmonic potential.

2.1.1 The atom-laser system

Consider an atom with two states $|0\rangle$ and $|1\rangle$, which are separated in energy by $\hbar\omega_a$. Using these states as the basis for a two-dimensional vector space, define the Pauli operators

$$\sigma_x \equiv \begin{bmatrix} 0 & 1 \\ 1 & 0 \end{bmatrix} \qquad \sigma_y \equiv \begin{bmatrix} 0 & -i \\ i & 0 \end{bmatrix} \qquad \sigma_z \equiv \begin{bmatrix} 1 & 0 \\ 0 & -1 \end{bmatrix} \tag{2.1}$$

and the atomic raising and lowering operators

$$\sigma^{+} = \frac{1}{2}(\sigma_x + i\sigma_y) = \begin{bmatrix} 0 & 1 \\ 0 & 0 \end{bmatrix} \qquad \sigma^{-} = \frac{1}{2}(\sigma_x - i\sigma_y) = \begin{bmatrix} 0 & 0 \\ 1 & 0 \end{bmatrix}. \tag{2.2}$$

The potential that confines the atom in free space can be approximated by a harmonic well with frequency ω_x where the atom has motional eigenstates $|n\rangle$. The harmonic raising and lowering operators are defined such that,

$$a^\dagger|n\rangle = \sqrt{n+1}|n+1\rangle \tag{2.3}$$

$$a|n\rangle = \sqrt{n}|n-1\rangle \tag{2.4}$$

An atom's hamiltonian in this situation is composed of two terms, the first representing the atom's internal two-state system and the second representing its motion in the harmonic potential.

$$H_0 = \frac{\hbar}{2}\omega_a\sigma_z + \hbar\omega_x\left(a^\dagger a + \frac{1}{2}\right) \tag{2.5}$$

Hamiltonian H_0 has eigenstates $|a,n\rangle$ where $a \in \{0,1\}$ is the atom's internal state and $n \in \{0,1,2,3...\}$ is its motional state, as shown in figure 2-1. Pulses of laser light directed along the x axis are used to manipulate and measure these states in our experiments. The interaction between the atom and a single-mode coherent light source has the hamiltonian[WMI+98],

$$H_I = \frac{\hbar}{2}\Omega\left(\sigma^+ + \sigma^-\right)\left[e^{i(kx-\omega_L t+\phi)} + e^{-i(kx-\omega_L t+\phi)}\right] \tag{2.6}$$

where the light source has angular frequency ω_L, phase ϕ, and wavenumber k. Ω is the interaction strength between the atom and the light field. The connection between H_I and the harmonic oscillator is made more explicit by noting that $x = x_0(a + a^\dagger)$, where $x_0 = \sqrt{\frac{\hbar}{2m\omega_x}}$ is a characteristic length scale for the atom's motion in the trap. m is the atom's mass. Defining the Lambe-Dicke factor $\eta \equiv kx_0$,

$$H_I = \frac{\hbar}{2}\Omega\left(\sigma^+ + \sigma^-\right)e^{i(\eta(a+a^\dagger)-\omega_L t+\phi)} + h.c. \tag{2.7}$$

H_I acts both on the atom's internal and motional states. For clarity, we can rewrite it in terms of the strength $\Omega_{n,m}$ with which light is coupled to each atomic transition

$|0,n\rangle \leftrightarrow |1,m\rangle$.

$$H_I = \frac{\hbar}{2}\sum_{n,m}\Omega_{n,m}e^{i(\phi-\omega_L t)}\left(\sigma^+ + \sigma^-\right)|m\rangle\langle n| + h.c. \tag{2.8}$$

where $\Omega_{n,m} \equiv \Omega\langle m|e^{i\eta(a+a^\dagger)}|n\rangle$. For the experiments described in this thesis, the atom is confined to a space much smaller than the wavelength of incident light so that $\eta \ll 1$. The exponent $e^{i\eta(a+a^\dagger)}$ can safely be expanded to first order in η, allowing us to calculate the relevant coupling coefficents $\Omega_{n,m}$.

$$\Omega_{n,n} = \Omega\left(1 - \frac{\eta^2}{2}(2n+1)\right) \tag{2.9}$$

$$\Omega_{n+1,n} = \Omega\eta\sqrt{n+1} \tag{2.10}$$

$$\Omega_{n-1,n} = \Omega\eta\sqrt{n} \tag{2.11}$$

It is often more natural to describe the interaction between the laser and atom in the Interaction Picture, where the frame of reference rotates with H_0 so that the atom's states are stationary in the absence of laser light. Defining $U = e^{iH_0 t/\hbar}$ and dropping the fast-rotating terms,

$$H_I' = U^\dagger H_I U = \frac{\hbar}{2}\sum_{n,m}\Omega_{n,m}e^{i(\phi-\delta t)}\sigma^+|m\rangle\langle n| + h.c. \qquad \delta \equiv \omega_L - \omega_a - (m-n)\omega_x \tag{2.12}$$

2.1.2 Resonant interactions in the atom's rotating frame

Resonant light ($\omega_L = \omega_a$) couples the $|0,n\rangle$ and $|1,n\rangle$ states. Such a transition that leaves n unchanged will be called a carrier transition. In this case, the Hamiltonian becomes:

$$H_I = \frac{\hbar}{2}\Omega_{n,n}\left(e^{i\phi}\sigma^+ + e^{-i\phi}\sigma^-\right) \tag{2.13}$$

The effect of a laser pulse of finite duration T is a rotation of the atom's state[1] by angle $\theta = \Omega T$, which will be discussed in more depth in section 2.2.

$$R(\theta, \phi) = \exp\left[-iH_I'T/\hbar\right] = \exp\left[-i\frac{\theta}{2}(e^{i\phi}\sigma^+ + e^{-i\phi}\sigma^-)\right] \tag{2.14}$$

When the laser is detuned such that $\omega_L = \omega_a + \omega_x$, it addresses the blue sideband transition $|0, n\rangle \leftrightarrow |1, n+1\rangle$. Much like a carrier pulse, a blue sideband pulse of duration T rotates the atomic and motional states simultaneously by an angle $\theta = \Omega_{n,n+1}T$.

$$R^+(\theta, \phi) = \exp\left[-iH_I'T/\hbar\right] = \exp\left[i\frac{\theta}{2}(e^{i\phi}\sigma^+ a + e^{-i\phi}\sigma^- a^\dagger)\right] \tag{2.15}$$

Similarly, the action of a red sideband pulse couples $|0, n\rangle$ and $|1, n-1\rangle$ with a rotation by $\theta = \Omega_{n,n-1}T$:

$$R^-(\theta, \phi) = \exp\left[-i\frac{\theta}{2}(e^{i\phi}\sigma^+ a^\dagger + e^{-i\phi}\sigma^- a)\right] \tag{2.16}$$

Because they manipulate the atomic and motional states in concert, sideband pulses are useful for the cooling, measurement, and control of the atom's quantum motion. Section 2.2.2 also examines the importance of the square-root dependence of θ on n during sideband pulses (see equation 2.10), which allows for conditional rotations of the atom's internal state.

2.1.3 Off-resonant interactions

A strong oscillating light field that is detuned from the atomic resonance introduces a small shift δ_{AC} in the transition's resonant frequency. This is often referred to as the AC or dynamical Stark shift. To first order[HGR+03],

$$\delta_{AC} = \frac{\Omega_{AC}^2}{\omega_L - \omega_a}. \tag{2.17}$$

[1]Because the atom is typically cooled to the ground state of its motion in our experiments, we approximate equation 2.9 as $\Omega n, n = \Omega$.

The Rabi frequency of the non-resonant light field , Ω_{AC}, is slower than Ω as non-resonant light is more weakly coupled to the transition:

$$\Omega_{AC}^2 = \Omega^2 - (\omega_L - \omega_a)^2. \tag{2.18}$$

A pulse of light tuned to the blue sideband, which is used to control the ion's motion, can couple off-resonantly to the carrier transition and introduce a systematic linear phase shift of

$$\phi_{AC} = \delta_{AC} T \tag{2.19}$$

between the atomic $|0\rangle$ and $|1\rangle$ levels. Here, T is the length of the pulse. This phase shift is clearly undesirable in experiments that demand coherent control of the atom's state, but fortunately it can be somewhat compensated by shifting the phase ϕ of the subsequent laser pulse by ϕ_{AC}.

Equation 2.13 becomes more complicated for off-resonant light due to the different rates of rotation of the laser (H_I) and atom (H_0) Hamiltonians. A more accurate compensation scheme for Stark shifts that reconciles the two different rotating frames is proposed in Labaziewicz's PhD thesis[Lab08], but was not implemented in time for the experiments in this current thesis.

2.2 Coherent manipulations of atomic states

After introducing a physical model for the trapped ion, the next phase of this chapter is to describe the trapped ion in the more general terms of quantum information. This section explains how resonant laser pulses can perform arbitrary unitary operations on the qubit formed by two atomic energy levels, and how the ion's quantized motion can used to store a second qubit in the strontium ion.

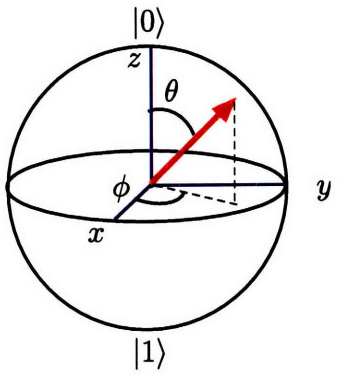

Figure 2-2: A state vector represented on the Bloch sphere.

2.2.1 A single qubit

Qubits are the fundamental units of quantum information. The general state of a qubit is

$$|\psi\rangle = a|0\rangle + b|1\rangle \tag{2.20}$$

where the complex coefficients a and b are normalized such that $|a|^2 + |b|^2 = 1$. Up to an overall phase that has no physical consequence, the state of a qubit can also be represented by two angles θ and ϕ:

$$|\psi\rangle = \cos\frac{\theta}{2}|0\rangle + e^{-i\phi}\sin\frac{\theta}{2}|1\rangle \tag{2.21}$$

It is helpful to visualize the state of the qubit as a vector of unit length, with direction defined by the angles θ and ϕ from the z-axis and x-axis respectively. This vector is constrained to point to locations on the surface of a unit sphere called the Bloch sphere, as shown in figure 2-2.

Coherent operations on a single qubit are represented by unitary 2×2 matrices acting on the vector space $\{|0\rangle, |1\rangle\}$. For example, the quantum NOT gate exchanges the coefficients a and b, performing the function of a classical NOT gate when the qubit is initially in one of its eigenstates.

$$NOT = \begin{bmatrix} 0 & 1 \\ 1 & 0 \end{bmatrix} \tag{2.22}$$

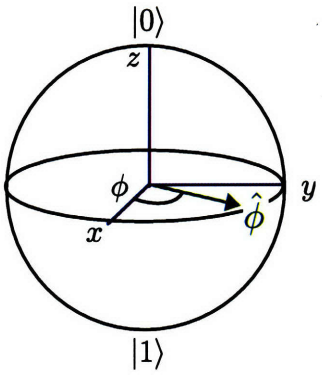

Figure 2-3: A carrier pulse $R(\theta, \phi)$ rotates the atom's state by an angle θ about $\hat{\phi}$.

This NOT gate happens to be identical to the Pauli matrix σ_x.

Our goal is to find a connection between coherent operations and resonant atom-light interactions, so that the atom's states can be controlled at a quantum level by laser pulses. In general [NC00], any unitary operation on the qubit can be written as a rotation of the state vector about an axis $\hat{n}$.

$$U = R_{\hat{n}}(\theta) = \exp\left[-i\frac{\theta}{2}\hat{n}\cdot\vec{\sigma}\right] \tag{2.23}$$

where $\vec{\sigma} = \sigma_x\hat{x} + \sigma_y\hat{y} + \sigma_z\hat{z}$. For example, the NOT gate can be written as $R_{\hat{y}}(\pi)$ up to an unobservable global phase. Furthermore, an arbitrary single-qubit rotation can in turn be represented by a series of rotations about only two fixed axes. In other words, there exist real numbers α, β, γ, and δ such that

$$U = e^{i\alpha}R_x(\beta)R_y(\gamma)R_x(\delta) \tag{2.24}$$

for any unitary operator U acting on a single qubit.

To see how laser pulses can be used to implement any unitary gate, recall from equation 2.14 that the action of a resonant laser pulse of phase ϕ and duration T can also be written as a rotation by angle $\theta = \Omega T$. The rotation is about an axis $\hat{n}$ in the $x - y$ plane that is separated from the x axis by an angle ϕ. Figure 2-3 shows an

example rotation on the Bloch sphere.

$$R(\theta,\phi) = \exp[-iH_I T/\hbar] = \exp\left[-i\frac{\theta}{2}(e^{i\phi}\sigma^+ + e^{-i\phi}\sigma^-)\right] \tag{2.25}$$

For appropriate values of ϕ, laser pulses can generate the x and y rotations required to build an arbitrary unitary operation using equation 2.24:

$$R_x(\theta) = R(\theta,0) = \exp\left[-i\frac{\theta}{2}\sigma_x\right] \tag{2.26}$$

$$R_y(\theta) = R(\theta,\frac{\pi}{2}) = \exp\left[-i\frac{\theta}{2}\sigma_y\right] \tag{2.27}$$

2.2.2 Multiple-qubit operations

The prototypical two-qubit gate is the controlled-NOT (CNOT) gate, which conditionally flips the state of a target qubit. With a combination of CNOT gates and single-qubit rotations, it is possible to perform arbitrary unitary operations on any number of qubits[NC00]. The CNOT can be represented by a matrix as,

$$U_{CNOT} = \begin{bmatrix} 1 & 0 & 0 & 0 \\ 0 & 1 & 0 & 0 \\ 0 & 0 & 0 & 1 \\ 0 & 0 & 1 & 0 \end{bmatrix} \tag{2.28}$$

which is expressed in the basis $\{|00\rangle, |10\rangle, |01\rangle, |11\rangle\}$. The first qubit is the target and the second is the control. The CNOT gate as it is written above does not lend itself easily to physical implementation. It can, however, be constructed from a controlled-phase gate, which is a form of the conditional rotation that was alluded to in the

previous discussion of sideband pulses.

$$U_{CPHASE} = \begin{bmatrix} 1 & 0 & 0 & 0 \\ 0 & 1 & 0 & 0 \\ 0 & 0 & 1 & 0 \\ 0 & 0 & 0 & -1 \end{bmatrix} \tag{2.29}$$

Continuing to define $R(\theta, \phi)$ as an independent rotation of the first qubit only (which is implemented using a carrier pulse),

$$U_{CNOT} = R(\frac{\pi}{2}, 0) U_{CPHASE} R(\frac{\pi}{2}, \pi) \tag{2.30}$$

The lowest two eigenstates of the atom's quantum motion can be used as a control qubit in the implementation of a CNOT gate using a single atom[CZ95]. To see how this works, recall that a laser pulse tuned to the blue sideband of the atomic resonance rotates the atom's internal and motional states simultaneously. The action of a pulse with duration T and phase ϕ is,

$$R^{+}(\theta, \phi) = \exp\left[i \frac{\theta}{2} (e^{i\phi} \sigma^{+} a + e^{-i\theta} \sigma^{-} a^{\dagger}) \right] \tag{2.31}$$

where $\theta = \Omega_{n,n+1} T = \left(\Omega \eta \sqrt{n+1} \right) T$. The internal atomic state is rotated by an angle θ on the Bloch sphere, which depends on n via $\Omega_{n,n+1}$ (see equation 2.10). Carefully selected pulse sequences can therefore perform conditional logic operations that use the motional state as a control qubit.

One problem with this scheme is that the same pulses that couple $|00\rangle$ to $|11\rangle$ will also couple $|01\rangle$ to $|12\rangle$, which is outside of the subspace of the atom's states in which we desire to operate. This subspace of the states of a harmonic oscillator, unlike the two-state system, is not closed under arbitrary rotations. However, it has been shown[CC01] that sideband rotations by $\theta = j\pi\sqrt{2}$ constrain the atom to the desired state space for integers j. Using this knowledge, a CNOT gate can be implemented

using carrier and blue sideband pulses on a single ion:

$$U_{CNOT} = R(\frac{\pi}{2}, 0) \underbrace{R^+(\frac{\pi}{\sqrt{2}}, \frac{\pi}{2}) R^+(\pi, 0) R^+(\frac{\pi}{\sqrt{2}}, \frac{\pi}{2}) R^+(\pi, 0)}_{U_{CPHASE}} R(\frac{\pi}{2}, \pi) \tag{2.32}$$

A similar sequence was used to implement a CNOT gate on two $^{40}Ca^+$ ions[SKHR+03].

An additional complication is introduced by off-resonant coupling to the carrier transition during sideband pulses (section 2.1.3). A phase shift accumulates between the atomic $|0\rangle$ and $|1\rangle$ states that is proportional to the total duration of previous pulses on the blue sideband. By shifting the phases subsequent laser pulses in the opposite direction, the effects of off-resonant coupling can be partially cancelled.

$$\begin{aligned} U_{CNOT} = R(\frac{\pi}{2}, 2\phi_\pi + 2\phi_{\pi/\sqrt{2}}) R^+(\frac{\pi}{\sqrt{2}}, \frac{\pi}{2} + 2\phi_\pi + \phi_{\pi/\sqrt{2}}) \\ \times R^+(\pi, \phi_\pi + \phi_{\pi/\sqrt{2}}) R^+(\frac{\pi}{\sqrt{2}}, \frac{\pi}{2} + \phi_\pi) R^+(\pi, 0) R(\frac{\pi}{2}, \pi) \end{aligned} \tag{2.33}$$

where $\phi_\pi = \frac{\pi}{\Omega_{0,1}} \delta_{AC}$ and $\phi_{\pi/\sqrt{2}} = \frac{\pi}{\Omega_{0,1}} \delta_{AC}$ are the phases accumulated during the π and $\pi/\sqrt{2}$ blue sideband pulses, respectively. We can measure their values with a Ramsey experiment, which is described in the next section.

Equation 2.33 shows the pulse sequence that will be used to demonstrate a controlled-NOT operation on a single $^{88}Sr^+$ ion in chapter 6. Such entangling operations between spin and motional states are important even in a system with many individual ions, because their collective motional modes are used as a form of communication.

2.3 Decoherence

The ultimate limit on coherence time is constrained by the lifetime of the atomic transition. In many cases, there are sources of decoherence in the experimental apparatus that prevent coherence times from reaching this limit. These errors can either come from a loss of information through undesired interactions with the atom's en-

vironment, or from errors communicated by the classical control system.

2.3.1 Experiments for measuring decoherence

This section presents a series of experiments that can be used to characterize decoherence processes. They are useful for understanding what types of scientific experiments are possible as well as for pinpointing ways that the apparatus could be improved.

Rabi oscillations

A resonant laser beam that is well-coupled to the atomic transition will drive coherent oscillations in the relative populations of the atomic states, as described in equation 2.13. These Rabi oscillations [Rab37] are often used as an initial demonstration of quantum control. The measurement procedure is simply to initialize the atom in state $|0\rangle$ and apply a pulse of duration T. The probability of finding the atom in the $|0\rangle$ state, which is the quantity measured in our experiments, should be given by

$$P_{|0\rangle}(T) = \cos^2(\Omega T/2) \tag{2.34}$$

In practice, decoherence causes the amplitude of the oscillations to decay as a function of T. This decay is often caused by instabilities in the Rabi frequency Ω, which in turn depends on the incident laser power as well as the detuning of the laser from resonance.

It is also useful to measure Rabi oscillations that are driven by blue sideband pulses, which address both the internal and motional states of the ion. Compared to carrier transitionions, coupling to sideband transitions is weaker by a factor of η. As a result, the Rabi oscillations are slower and coherent manipulations of motional states using sideband pulses are more likely to run up against the limitations imposed by short coherence times. This makes the blue sideband Rabi frequency $\Omega_{n,n+1}$ worth knowing when planning experiments.

Ramsey interferometry

Experiments based on Ramsey interferometry [KPRS50, LGRS04] are an important tool for investigating noise in the classical control system as well as for calibrating the phase shift corrections for AC Stark shifts.

The most basic Ramsey experiment is used to measure the frequency stability of the laser. First, the atom's internal state[2] is initialized in the $|0\rangle$ state. A $\pi/2$ pulse rotates the atom into the $(|0\rangle + |1\rangle)/\sqrt{2}$ state. During the subsequent period of free evolution, detuning of the laser from resonance causes the atom to precess in the laser's rotating frame. The accumulated phase ϕ between laser and atom is then transferred to the population of the atomic state with a second $\pi/2$ pulse. We can write the pulse sequence mathematically as

$$R(\frac{\pi}{2}, 0)\tau R(\frac{\pi}{2}, 0) \tag{2.35}$$

where τ is the length of the free evolution period. The population of the $|0\rangle$ state at the end of the experiment is $\frac{1}{2}(1 + \cos(\phi))$. For a constant detuning of the laser, ϕ is proportional to τ and the florescence signal oscillates sinusoidally with τ – generating the famous "Ramsey fringe" pattern. Fluctuations in the laser-atom phase, originating for example in drifts of the laser's frequency during the free evolution period, cause a decay in the amplitude of the Ramsey fringes with a time constant of T_2^*

Ramsey interferometry can also be used to find the phase shift $\phi_{AC} = \delta_{AC}\tau$ induced by a blue sideband pulse due to the AC Stark effect. The result of this measurement is used in pulse sequences to offset the AC Stark effect, as demonstrated in equation 2.33. In this experiment the total time between the $\pi/2$ pulses remains constant and the length of a sideband pulse is scanned:

$$R(\frac{\pi}{2}, 0)\tau R^{\delta}(\Omega_{AC}(1-\tau), 0)R(\frac{\pi}{2}, 0). \tag{2.36}$$

Here, $R^{\delta}(\theta, \phi)$ is a pulse that is neither resonant with the carrier nor the blue sideband,

[2]The quantum motion is cooled to its ground state for all experiments involving only manipulation of the internal state, so I will omit the second qubit from these equations to lighten the notation.

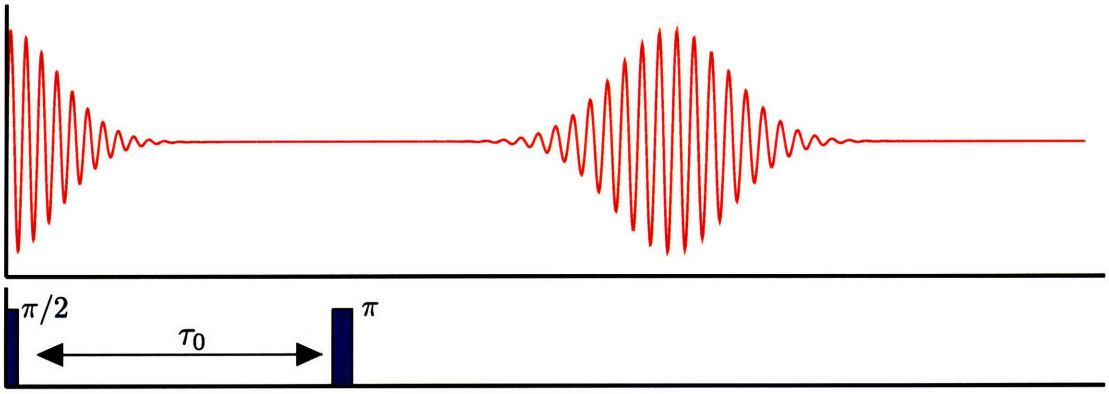

Figure 2-4: Recovery of phase coherence with a spin echo. Top: measured population of the $|0\rangle$ state vs. time. Bottom: the pulse sequence. A second $\pi/2$ pulse at a variable time $\tau + \tau_0$ must be added to prepare the state for measurement.

but is detuned from the carrier by δ. The population of the $|00\rangle$ state evolves as $\frac{1}{2}(1 - \cos(\delta_{AC}\tau))$. Using equation 2.17, the phase shift at the sideband frequency can be extrapolated by measuring the effect of off-resonant pulses at several frequencies.

Spin-echo recovery

The decay of phase coherence with time limits our ability to control the ion's state. For certain types of noise, phase coherence can be recovered with a spin echo long after the original decay with the judicious insertion of a π pulse into the pulse sequence [Hah50].

$$R(\frac{\pi}{2}, 0)\tau R(\pi, 0)\tau_0 R(\frac{\pi}{2}, \pi) \tag{2.37}$$

Consider the case where $\tau = \tau_0$. During the free evolution period of a Ramsey experiment with no laser detuning, the state of the atom should remain stationary. Errors in the laser's frequency cause an undesired precession of the atom's state in the laser's frame. A π pulse inserted in the middle of the free evolution period reverses the direction of the precession, effectively canceling the effect of a constant frequency error. When scanning τ, an echo of the orignal signal reappears centered at $\tau = \tau_0$, as shown in figure 2-4.

The amplitude of the recovered signal will decay exponentially with a time constant of T_2^* as τ_0 increases. By scanning the length of both time delays in concert we

can come close to directly measuring T_2.

$$R(\frac{\pi}{2},0)\tau R(\pi,0)\tau R(\frac{\pi}{2},\pi) \tag{2.38}$$

This spin-echo technique can only recover from noise that is effectively constant over the length of τ. If the phase is refocused more frequently using the Carr-Purcell sequence[CP54], and the dominant noise sources are slower than time between the echoes, it is possible to extend the coherence time even further:

$$R(\frac{\pi}{2},0)\frac{\tau}{2n}R(\pi,0)\frac{\tau}{n}R(\pi,0)\frac{\tau}{n}...R(\pi,0)\frac{\tau}{n}R(\pi,0)\frac{\tau}{2n} \tag{2.39}$$

where the spin is echoed n times. This sequence is used in chapter 6 to measure T_2.

2.3.2 Minimizing decoherence with composite pulses

Imperfections in the classical control of a quantum system are inevitable in any realistic experimental situation. Fortunately, sequences of consecutive pulses can be designed that are self-correcting in the face of many common control errors [Lev86]. The use of these composite pulses has been fantastically successful in NMR experiments, but their applicability can often be extended to the quantum control of any two-level system[VC05].

In this thesis, we are curious to see if we can make use of one particularly popular type of composite pulse called BB1[Wim94]. Systematic errors in laser amplitude or pulse length can distort any rotation by θ into a rotation by $\theta[1+\epsilon]$. BB1 composite pulses experience a reduced distortion of $\theta[1+\mathcal{O}(\epsilon^3)]$, without requiring any prior knowledge of the magnitude of the error. For a desired rotation of $R(\theta,0)$, the corresponding BB1 composite pulse can be generated algorithmically:

$$R_{BB1}(\theta) = R(\pi,\phi)R(2\pi,3\phi)R(\pi,\phi)R(\theta,0) \tag{2.40}$$

where $\phi = \cos^{-1}(-\theta/4\pi)$.

Figure 2-5 shows the trajectories of a composite $\pi/2$-pulse in the presence of

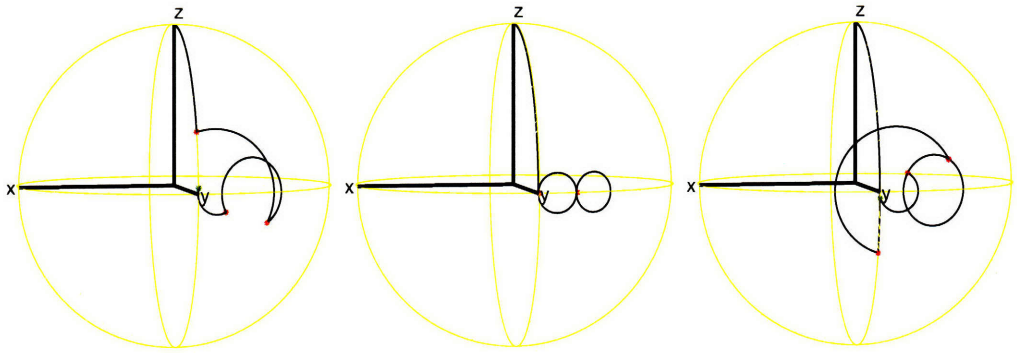

Figure 2-5: The trajectories of a spin driven by a BB1 composite pulse in with 25% under-rotation error (left), no systematic rotation error (center) and a 25% over-rotation error. Reproduced with permission from [VC05].

systematic errors that cause over- or under-rotation. The first step of the trajectory is the uncorrected pulse, $R(\theta, 0)$. Even for errors as large as 25%, it is clear that BB1 can make a big difference. This is tested experimentally in chapter 6. As the functionality of BB1 composite pulses is already well-established, our goal is instead to diagnose the level of laser amplitude noise in the experiment: if the composite pulses outperform uncorrected pulses, it indicates an area where the apparatus would benefit from an upgrade.

2.4 The $^{88}Sr^{+}$ ion

Singly-ionized strontium is the ion of choice for our experiments. It has a single electron and no nuclear spin, resulting in a simple hydrogenic energy structure. The quadrupole transition from $4D_{5/2}$ to $5S_{1/2}$ has an exceptionally long lifetime of 345ms with a corresponding natural linewidth of only 0.4Hz, making it an excellent qubit candidate. An additional advantage of using $^{88}Sr^{+}$ is that all of the relevant transitions are accessible to diode lasers, which allows a more straightforward experimental apparatus (appendix A).

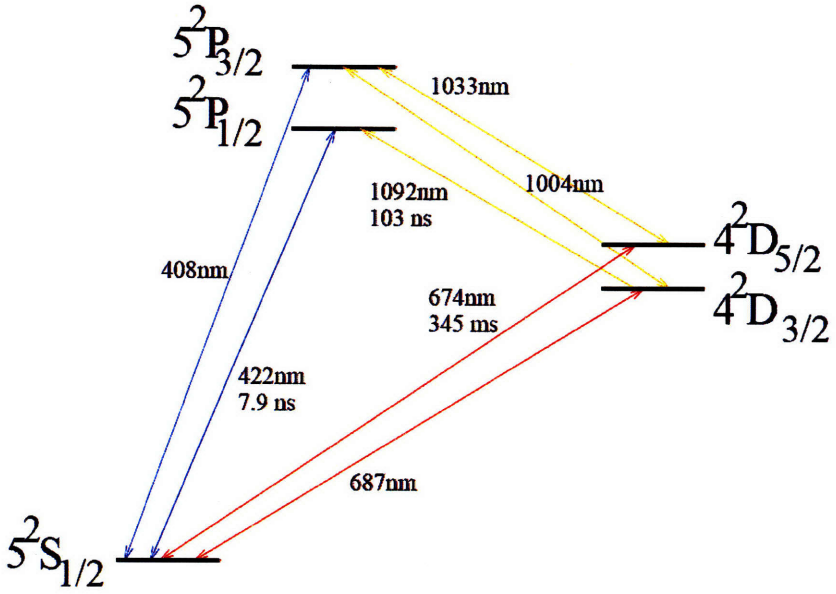

Figure 2-6: The energy levels of $^{88}Sr^{+}$ that are encountered in this thesis. Reproduced with permission from [Ric08]

2.4.1 Electronic energy levels

Figure 2-6 shows the energy levels of $^{88}Sr^{+}$ that are relevant to the experiments in this thesis. Coherent manipulations are performed on the $4D_{5/2} \leftrightarrow 5S_{1/2}$ quadrupole transition. More specifically, the $4D_{5/2}(m = -\frac{5}{2})$ and $S_{1/2}(m = -\frac{1}{2})$ Zeeman sublevels[3] are used as the $|1\rangle$ and $|0\rangle$ states of a qubit.

The $4D_{5/2}$ metastable state has a very long lifetime of 345ms, which sets a high upper bound for the number of consecutive quantum operations that could theoretically be performed coherently. In current experiments however, a much lower limit is imposed by frequency fluctuations in the 674nm qubit laser; the natural linewidth of the atomic transition is 0.4Hz, fifteen orders of magnitude smaller than the frequency of the incoming light. Because our desire for long coherence times places such strict demands on this classical control system, the construction of an additional frequency stabilization system for the 674nm laser is a major component of this thesis. Its design is described in chapter 3 and its performance is characterized in chapter 4.

[3]The $4D_{5/2}$ level is separated into $m = \{\pm\frac{1}{2}, \pm\frac{3}{2}, \pm\frac{5}{2}\}$ and the $5S_{1/2}$ level into $m = \{\pm\frac{1}{2}\}$ sublevels by a magnetic field.

An additional laser at 1033nm is used during state initialization to pump the ion from $4D_{5/2}$ to $4P_{3/2}$, which rapidly decays to the $5S_{1/2}$ ($|0\rangle$) state. The atom can alternatively be initialized in the $4D_{5/2}$ ($|1\rangle$) state by applying a π pulse with the 674nm laser after the ion has been pumped to $5S_{1/2}$.

In addition to having a qubit with a long coherence time, the $^{88}Sr^{+}$ energy level structure offers a relatively straightforward measurement scheme. The $5P_{1/2}$ excited state rapidly decays to the $5S_{1/2}$ ground state with a lifetime of 7.9ns, emitting a single photon each time. If the ion is initially in the S state, resonant 422nm light drives it to cycle rapidly between S and P and emit a bright florescence signal. No florescence is observed when the ion is shelved in the D state. Each measurement, which returns a binary value based on a threshold for the strength of the florescence signal, projects the atom's state onto $4D_{5/2}$ or $5S_{1/2}$. The relative probability of finding the atom in the S state is estimated from the average outcome of 100 identical state preparations and subsequent measurements.

From the $4P_{1/2}$ state, the ion decays to the metastable $4D_{3/2}$ state with a probability of 1/14 and disrupts the cycling of the 422nm $S \leftrightarrow P$ transition. A laser at 1092nm is therefore necessary to repump the ion back to the $4P_{1/2}$ state. This is useful both during state readout and when the 422nm transition is used for Doppler cooling.

2.4.2 Laser cooling

Uncontrolled thermal motion of the ion in the trap broadens the atomic resonances and prevents the internal states from being manipulated coherently. At the beginning of each measurement, lasers cool the ion to the ground state of its quantum motion in the ion trap's harmonic pseudopotential. After laser cooling [WDW78, NHTD78], the ion's motion can be controlled coherently by sideband pulses of the 674nm laser. The motional state then becomes quite useful as a second qubit, as described in section 2.2.2.

Laser cooling is performed in two stages. First, the 422nm laser is detuned to the red of the $5S_{1/2} \leftrightarrow 5P_{1/2}$ transition to Doppler cool the atom. Light is Doppler-

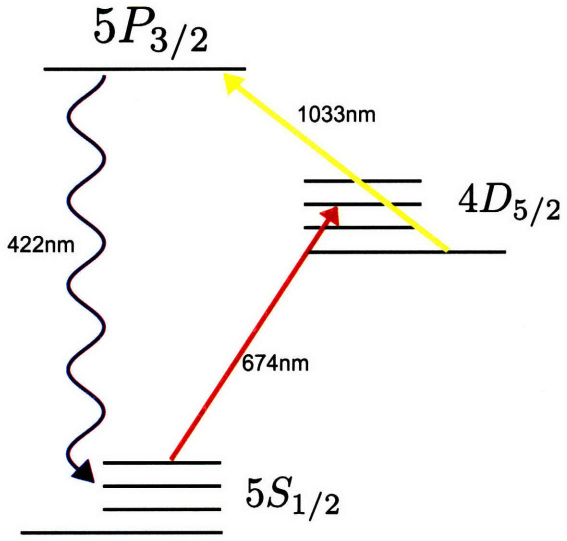

Figure 2-7: Sideband cooling.

shifted onto resonance for atoms moving towards the laser beam. The absorption of a resonant photon with wavenumber k imparts a momentum $\hbar k$ in the opposite direction of the atom's motion. When the photon is spontaneously re-emitted, the atom recoils in a random direction. On average, the atom's velocity is slowed down by each interaction with a photon.

After Doppler cooling, the thermal broadening of the $4D_{5/2} \leftrightarrow 5S_{1/2}$ transition is reduced to the point where motional sidebands can be spectrally resolved. The red 674nm laser is then used to sideband cool the atom to the ground state of its motion according to the diagramm in figure 2-7. The laser drives an ion from the $|S, n\rangle$ to the $|D, n-1\rangle$ state, removing one motional quanta. Because the lifetime of the metastable $4D_{5/2}$ state is so long, the 1033nm laser is used to pump the ion into the $5P_{3/2}$, which has a much shorter lifetime and decays rapidly to the $5S_{1/2}$ ground state. This cycle is repeated until the ion is cooled to the ground state of its motion with $n = 0$.

2.5 Summary

This chapter showed how the basic elements of quantum control can be implemented by using pulses of laser light to address the internal and motional states of a $^{88}Sr^{+}$

ion. A theoretical description of the interaction of ions with light was presented in the first section, which was then translated into the language of quantum information in the second section. There, the use of the ion's quantum motion as a second qubit was described. The next section was dedicated to understanding the behavior of quantum information in less-than-ideal experimental conditions. Experimental techniques for investigating decoherence and mitigating its effects were presented. In the final section, we saw how the energy level structure of $^{88}Sr^{+}$ provides the narrow qubit transition and efficient readout scheme that make these experiments possible.

Chapter 3

Stabilization of the 674nm Qubit Laser to a Fabry-Perot Cavity: Theory and Design

Our desire to implement sequences of coherent quantum logic operations places strict demands on the precision of the classical control system. In this chapter, I describe the theory and design of an electronic feedback system that locks the 674nm qubit laser's frequency to the resonance of a high finesse Fabry-Perot etalon using the popular Pound-Drever-Hall (PDH) technique [Bla00, ZH92]. This lock significantly extends the capabilities of the existing laser system [LRB+07] by providing a second stage of frequency stabilization.

The chapter begins with a theoretical discussion of PDH laser locks in section 3.1. Then, section 3.2 contains a detailed description of the construction and design of the entire feedback system. Chapter 4 describes the characterization of the lock, and analyzes the laser's frequency stability relative to the optical cavity. In chapter 5, the laser is put to the test with a series of experiments that measure the improved coherence time of the optical strontium qubit.

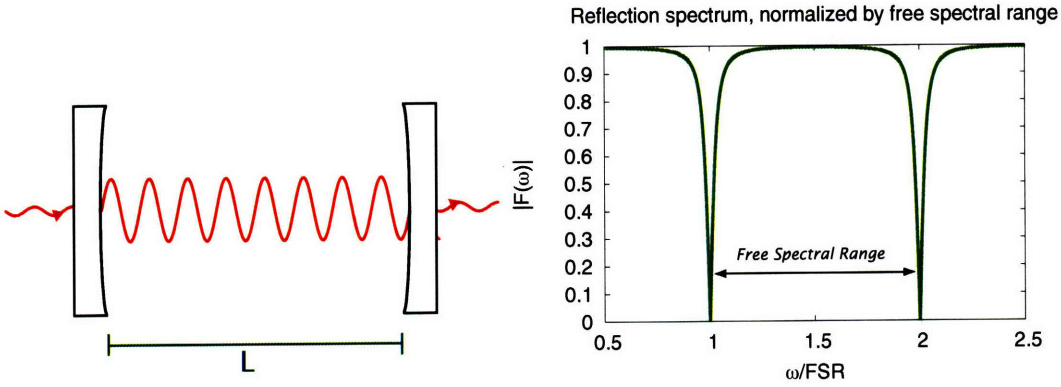

Figure 3-1: Left: A standing wave in a Fabry-Perot etalon. Right: The reflection spectrum for an etalon with mirror reflectivity $\mathcal{R} = 0.9$. The reflected amplitude drops to zero for resonant light, which is completely transmitted through the cavity. Such resonances occur periodically, whenever an integer number of wavelengths fits exactly between the mirrors. The distance between these resonances is called the free spectral range, ν_{FSR}.

3.1 Theory

The Pound-Drever-Hall (PDH) technique enjoys broad application wherever extremely stable optical frequency sources are required, including gravitational wave interferometers [AAD+92], precision spectroscopy [LHN+07], and the development of optical atomic clocks [OBS+07]. The PDH scheme employs lock-in detection to compare a laser's frequency to the resonance of a Fabry-Perot etalon, which decouples the laser's frequency and amplitude noise. Another feature of this detection method is that the error signal is approximately linear with frequency deviations from resonance, allowing the use of straightforward control techniques to suppress noise in the laser.

3.1.1 The Fabry-Perot Cavity as a Frequency Reference

For our purposes, a Fabry-Perot etalon is a resonant optical cavity formed by two parallel mirrors that face each other. Light shines into the cavity along the axis that connects the two mirrors. When an integer number of wavelengths fits exactly between these mirrors, light constructively interferes so that a standing wave forms inside the cavity. Some of this light then leaks back out through the mirrors at the same intensity as it is being injected by the laser. On resonance, this leakage beam is

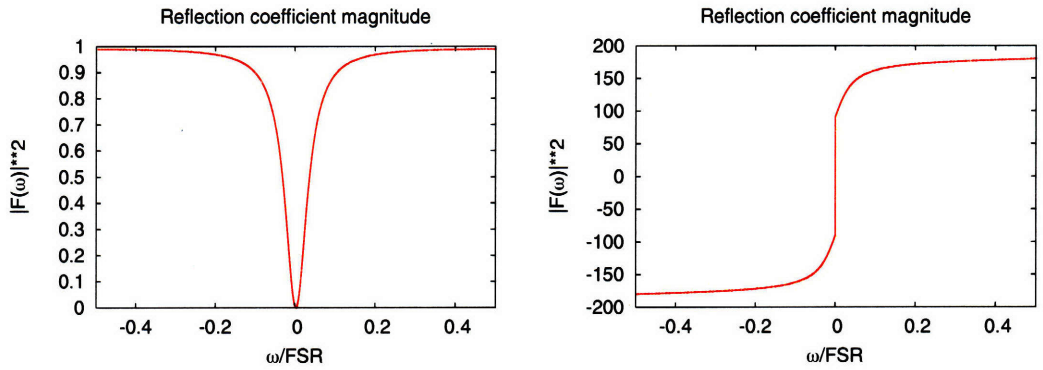

Figure 3-2: The magnitude and phase of the light reflected from a Fabry-Perot etalon near resonance.

exactly 180° out of phase with the directly reflected beam; the total reflected power is zero due to destructive interference. Such resonances occur periodically as shown in figure 3-1. Their frequency separation is given by the Free Spectral Range (FSR):

$$\nu_{FSR} = \frac{c}{2L} \tag{3.1}$$

where L is the mirror separation distance and c is the speed of light. Far from resonance, very little power can build up inside of the cavity and subsequently leak out to interfere with the directly reflected beam. Therefore, all of the off-resonant light is reflected from the cavity.

The reflection spectrum is more fully described by the etalon's complex reflection coefficient $F(\omega')$, which is the ratio of reflected and incident electric fields. Here, ω is the laser's frequency, and ω_0 is a resonant frequency of the etalon. For convenience, we can write the detuning of the laser from resonance as $\omega' = \omega - \omega_o$.

$$F(\omega') = \frac{E_{reflected}}{E_{incident}} = \frac{\mathcal{R}\left(\exp(i\frac{\omega'}{\nu_{FSR}})\right)}{1 - \mathcal{R}^2\exp(i\frac{\omega'}{\nu_{FSR}})} \tag{3.2}$$

where $\mathcal{R}$ is the mirror reflectivity. The intensity and phase of the reflection coefficient is plotted in figure 3-2.

A common metric for the quality of a Fabry-Perot cavity is its finesse $\mathcal{F}$, which is

the the ratio of the free spectral range ν_{FSR} to the resonance linewidth $\Delta\nu$:

$$\mathcal{F} = \frac{\nu_{FSR}}{\Delta\nu} = \frac{c}{2L\Delta\nu} = \frac{2\pi\tau c}{2L} \tag{3.3}$$

where τ is the lifetime of a photon in the cavity. A high finesse indicates that resonant photons bounce between the mirrors many times before escaping, constructively interfering to build up a large amount of power in the optical cavity. As mirror reflectivity approaches unity, the finesse is well approximated by

$$\mathcal{F} = \frac{\pi\sqrt{\mathcal{R}}}{1-\mathcal{R}} \approx \frac{\pi}{(1-\mathcal{R})^2} \tag{3.4}$$

It is clear from the above equations that highly reflective mirrors are the key to making a Fabry-Perot etalon with spectrally narrow resonances. The stability of the resonance frequency, on the other hand, relies on a perfectly constant mirror separation distance. Mechanically stable optical cavities with highly reflective mirrors can have reliable, spectrally narrow resonances and act as excellent frequency references.

3.1.2 Pound-Drever-Hall Locking

Armed with an understanding of the inner workings of Fabry-Perot etalons, we now turn our attention to the question of how to employ such frequency references in the stabilization of lasers. The following section is largely based on a derivation from Black's review paper [Bla00] on the same topic.

Generation of the error signal

Looking back to the plot of the reflection coefficient F in figure 3-2, notice that the intensity of light reflected from a Fabry-Perot cavity is symmetric about each resonance. The intensity of reflected light can only reveal the *magnitude* of the laser's deviation from resonant frequency, but has nothing to say regarding which *direction* the laser's frequency must be adjusted to correct the error. The phase of the reflected light, however, is an odd function across the resonance – this is precisely what we

need.[1]

To encode the phase of F into the reflected laser beam, the phase of the incident light is itself modulated at a frequency Ω that is much larger than the resonance linewidth. The resulting electric field takes the following form:

$$E_{inc} = E_0 e^{i(\omega' t + \beta \sin(\Omega t))} \approx E_0 \left[J_0(\beta) e^{i\omega' t} - J_1(\beta) e^{i(\omega' - \Omega)t} + J_1(\beta) e^{i(\omega' + \Omega)t} \right] \quad (3.5)$$

where J_0 and J_1 are Bessel functions, and β represents the strength of the phase modulation. The incident beam is now composed of three separate beams: a carrier oscillating at the laser frequency ω, and two sidebands at $\omega \pm \Omega$. After reflection from the etalon, each of these three beams is multiplied by the complex reflectivity coefficient, F, at their respective frequencies (recall that F was defined in equation 3.2).

$$E_{ref} = E_0 \left[F(\omega') J_0(\beta) e^{i\omega' t} - F(\omega' - \Omega) J_1(\beta) e^{i(\omega' - \Omega)t} + F(\omega' + \Omega) J_1(\beta) e^{i(\omega' + \Omega)t} \right] \quad (3.6)$$

When a photodiode measures the intensity of the reflected light, $I_{ref} = |E_{ref}|^2$, the carrier and sideband peaks interfere. This generates beat signals at DC, Ω, and 2Ω as well as an assortment of optical frequencies. The beat signal's intensity at the modulation frequency Ω contains the sought-after phase information:

$$I_{err}(t) = -2 J_0(\beta) J_1(\beta) |E_0|^2 Im \left\{ F(\omega') F^*(\omega' + \Omega) - F^*(\omega') F(\omega' + \Omega) \right\} \sin(\Omega t) \quad (3.7)$$

Once I_{err} is detected in the photodiode, the signal can be demodulated to yield the DC signal shown in figure 3-3. The full detection process will be described in the next section – but first, let us admire this PDH error signal for a moment. Very close to resonance, the reflection coefficient F and error signal I_{err} becomes linear

[1]Another common solution to this dilema is to lock the laser's frequency to a side of the etalon's resonance peak, where a small shift in the laser's frequency generates a large change in reflected light intensity. This approach is problematic because fluctuations in laser amplitude have an identical effect on the reflected power as do fluctuations in frequency.

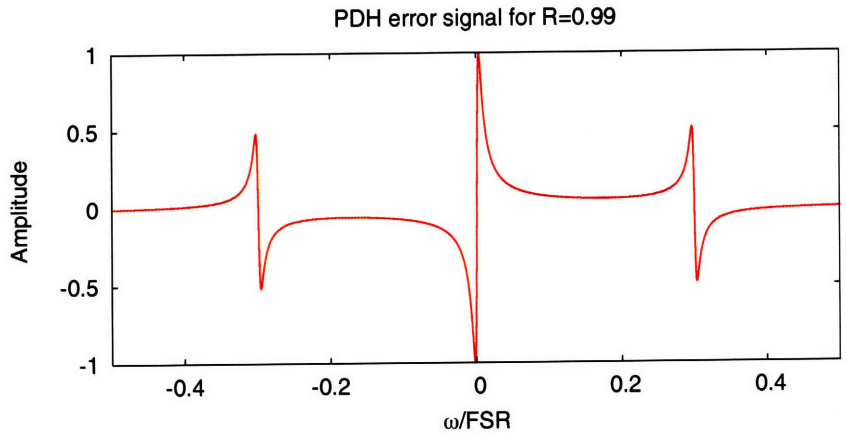

Figure 3-3: The PDH error signal as a function of the laser detuning ω', for a cavity with finesse around 300. The three resonances are spaced by the modulation frequency Ω. A higher finesse cavity, like the one used in this thesis, will have much narrower resonances in comparison to the distance between the carrier and sideband signals.

with frequency:

$$F(\omega') \approx \frac{i}{\pi}\frac{\delta\omega'}{\Delta\nu} \tag{3.8}$$

The error signal is also linear near resonance, making it straightforward to employ traditional control techniques such as PID feedback for holding the laser's frequency constant:

$$I_{err} \approx -\frac{4J_0(\beta)J_1(\beta)|E_0|^2}{\pi}\frac{\delta\omega}{\Delta\nu} \tag{3.9}$$

Since the lock typically has enough gain to hold the laser's frequency in this linear region, the slope of the error signal on resonance gives a good measure of the system's sensitivity to frequency shifts. To optimize the sensitivity, one can make the error signal taller by aligning light very well to the cavity mode and optimizing the modulation depth β to be 0.4 [Bla00]. The width of this linear region, which we would seek to minimize, is approximately equal to the cavity's spectral linewidth. A Fabry-Perot cavity with very high finesse is therefore an important component of the detection system.

Another important quality of a Fabry-Perot cavity is the stability of its reference frequency, which is controlled by the mirror spacing L. Equation 3.9 assumed that L was constant. For fluctuations δL in the cavity spacing and $\delta\omega$ in the laser's frequency,

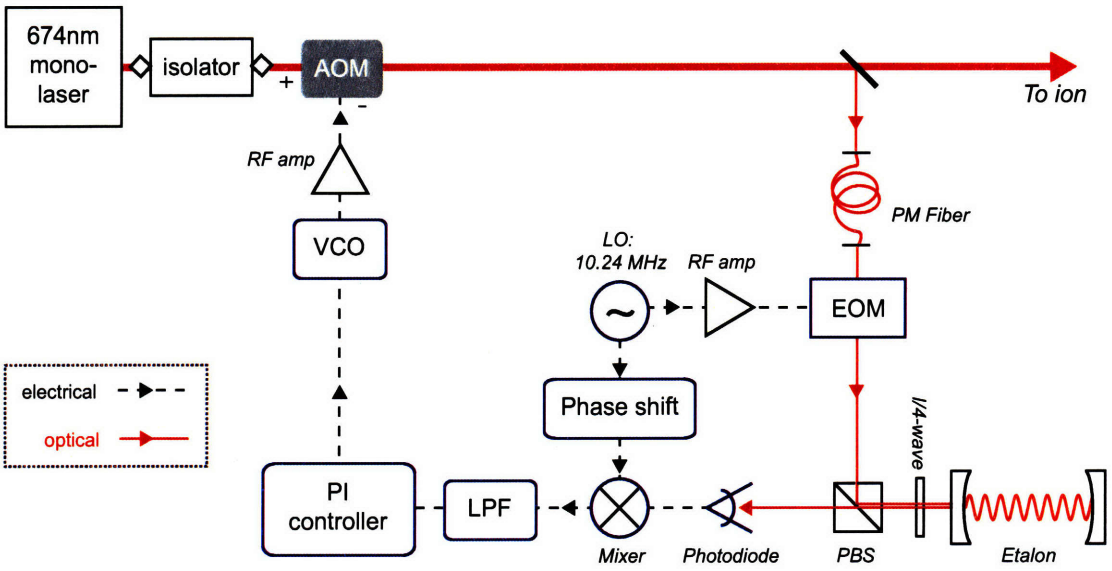

Figure 3-4: Design overview: the PDH lock loop. The light from the existing laser (which I call the monolaser) passes through an optical isolator and then an Acousto-Optic Modulator (AOM), which the lock uses to shift the laser's frequency to subtract errors. A small portion of the main beam is sampled and sent through a polarization-maintaining fiber to and Electro-Optica Modulator (EOM), which modulates the laser's phase at 10.24 MHz. A polarizing beamsplitter cube reflects the modulated light to the optical reference cavity, which has its polarization rotated by passing through a $\lambda/4$ plate twice so that light from the cavity is transmitted to a photodiode. From there, a mixer picks out the error signal carried at 10.24 MHz and sends it through a low-pass filter (LPF) to a servo controller. The DC control signal is translated by a Voltage-Controlled Oscillator (VCO) into a sine wave that drives the AOM's frequency correction of the laser.

the error signal can be rewritten:

$$I_{err} \approx -8J_0(\beta)J_1(\beta)|E_0|^2\frac{2L\mathcal{F}}{\lambda}\left[\frac{\delta\omega}{\omega}+\frac{\delta L}{L}\right] \tag{3.10}$$

We see that fluctuations in the cavity length masquerade as fluctuations in the laser's frequency. In order to effectively stabilize the laser's frequency, the cavity's length must also be extremely well-controlled. Two major sources of distortion in the cavity's length are acoustic vibrations [CHY+06] and thermal fluctuations [NML+06].

3.2 Design and Construction

The previous section described the theory behind PDH locking. In this section, I show the design for the laser lock that was implemented in our apparatus. A high-level diagram of the PDH laser stabilization system is shown in figure 3-4. A small sample of polarized 674nm laser light is sent through a single-mode fiber to a small optics breadboard that is rigidly mounted to a vacuum chamber that holds the optical cavity. The light first passes through an electro-optic modulator (EOM), which is driven at 10.24 MHz by a local oscillator to modulate the laser's phase as described in equation 3.5. A polarizing beam splitter reflects the light into the etalon. Since the reflected light passes twice through a $\lambda/4$ plate, its polarization is rotated by 90° before it returns to the beamsplitter where it can now be transmitted to a photodiode.

When the 10.24 MHz photodetector signal is mixed with the 10.24 MHz local oscillator, a DC error signal is generated which indicates the laser's distance from the Fabry-Perot resonance frequency (shown in figure 3-3). This error signal is then fed to a PI controller, which adjusts the laser's frequency by driving an acousto-optic modulator (AOM) via a voltage-controlled oscillator.

More details on each of the laser lock's subsystems are given in the remainder of this section.

3.2.1 The Optical Reference Cavity

The Fabry-Perot etalon is formed by two highly reflective mirrors that are optically contacted to a cyllindrical 10 cm spacer made from ultra-low expansion (ULE) glass. It was manufactured by AT Films in Longmont, CO. The center of the spacer is hollow with a small vent halfway between the mirrors, so that the optical path can be pumped out to vacuum pressure. The manufacturers provided a schematic, which is shown in figure 3-5. To confine a gaussian beam in the cavity, one mirror is curved with a radius of 500mm and the other is flat. Light is focused into the cavity such that the beam waist falls at the flat mirror and the wavefront has a radius of curvature of 500mm when it strikes the curved mirror.

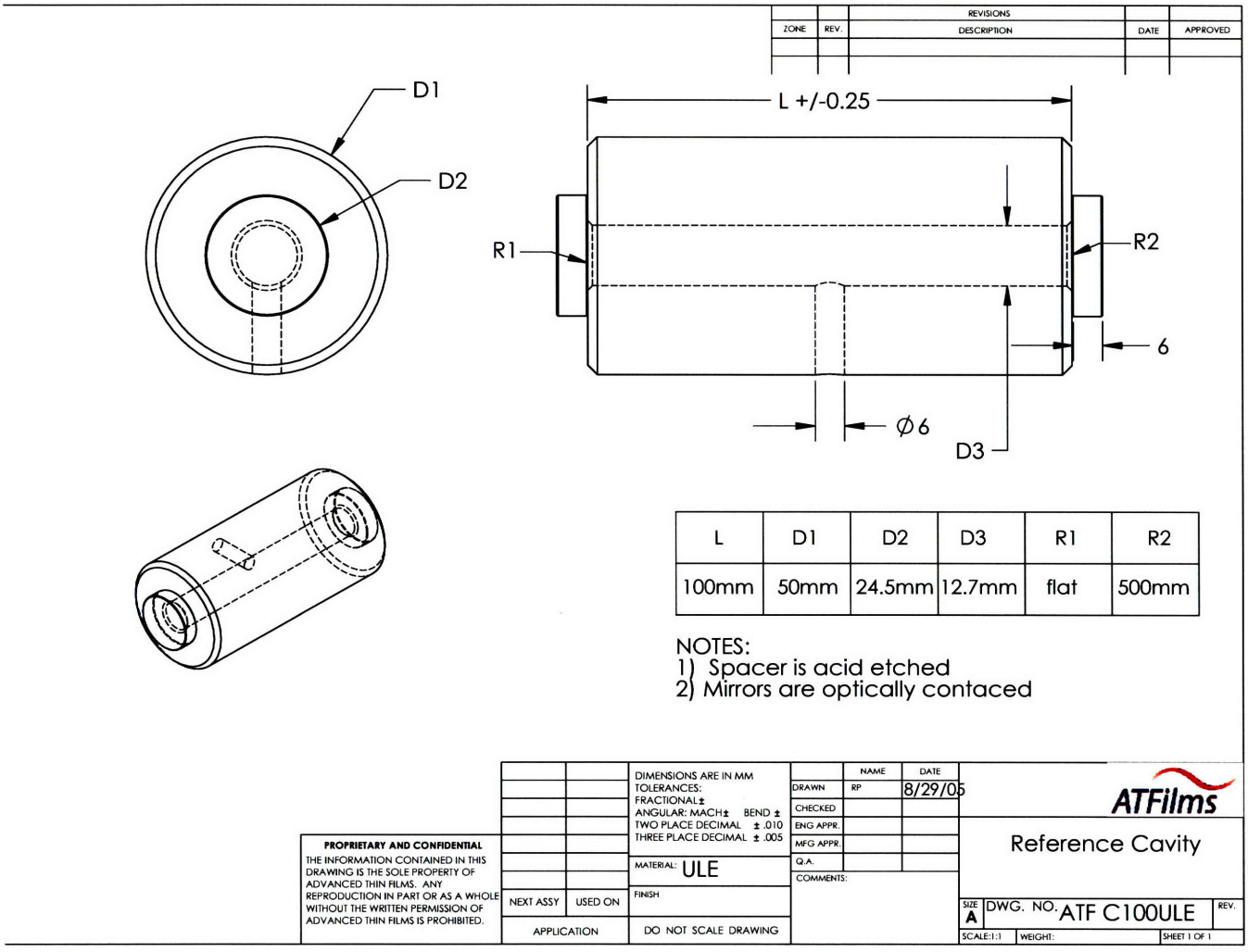

Figure 3-5: A schematic of the optical reference cavity, courtesy of ATFilms.

In equation 3.10 we saw that changes in this spacer's length shift the cavity's resonance, which is clearly undesirable.

$$I_{err} \propto \left[\frac{\delta\omega}{\omega} + \frac{\delta L}{L}\right] \tag{3.11}$$

For our laser frequency of $\omega = 2\pi \cdot 440$ THz and a cavity length $L = 10$ cm, a fluctuation in mirror separation of $\delta L = 0.1$ picometer has the same effect as a laser frequency fluctuation $\delta\omega = 2\pi \cdot 0.44$ kHz. It is extremely important that the cavity's length be as stable as possible. Thermal length fluctuations certainly exist on this scale even with ULE material, so the cavity's environment is actively temperature controlled. It is also essential to isolate the cavity from vibrations that might stretch the mirror separation distance. The design of the cavity's housing is designed with this in mind, based on many helpful suggestions found in [NMYH05].

The etalon is mounted vertically by a copper ring affixed to its center using torseal, as shown in figure 3-6. This copper ring is supported by three teflon rods, which aid in both vibrational and thermal isolation. A thin, cyllindrical copper sheath surrounds the cavity to prevent thermal gradients from developing. On the outside of this copper shell, there is a small sensor to measure the cavity's temperature. An aluminum shell wrapped in heater wire surrounds the whole copper assembly. This entire system is then placed in a vacuum chamber, which is evacuated by an ion pump.

A unique feature of this temperature control system is the sensor made from a quartz crystal whose oscillation frequency is sensitive to temperature. Unlike a thermistor, this sensor has a negligible calibration drift over many years – an attractive feature for a system entombed in a vacuum enclosure. It is also less sensitive to ambient electrical noise. The quartz oscillator circuit shown in figure 3.2.1 is designed as a Pierce oscillator with a buffered output, generating a square wave whose frequency changes linearly with temperature. A Field Programmable Gate Array (FPGA) then measures the frequency and uses a PI controller to adjust the heater power.

A small optics breadboard is rigidly attached to the vacuum chamber that contains the optical cavity's mount. The optics on this board are responsible for modulating

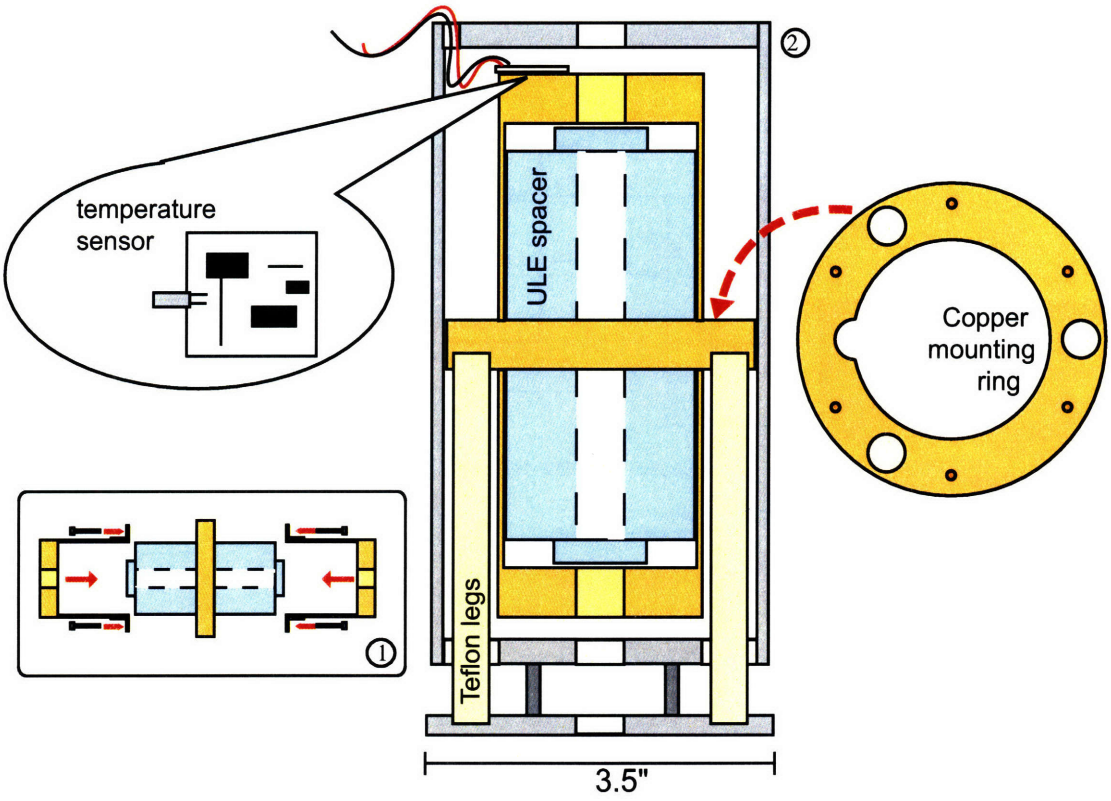

Figure 3-6: The optical cavity mounting scheme. (1) The two halves of the cyllindrical copper sheath that surrounds the cavity are attached to the center mounting ring with screws. (2) The full assembly suspends the cavity by its copper mounting ring on three hollow teflon rods. Heater wire is wrapped around the outer aluminum layer. Center diagram is to scale.

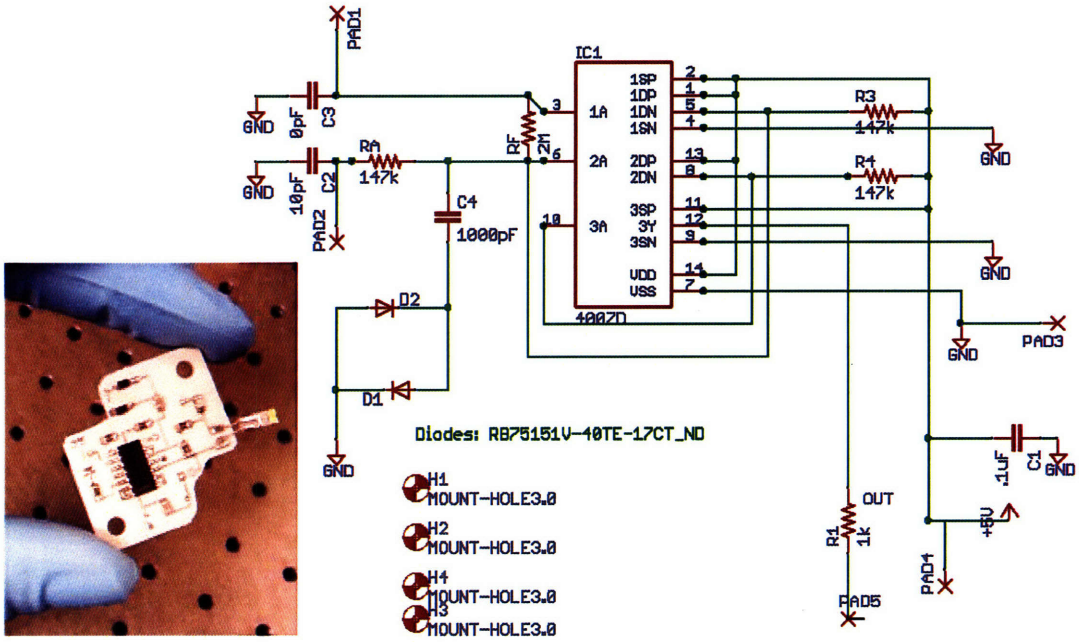

Figure 3-7: The quartz crystal temperature sensor is a Pierce oscillator with an output buffered by CMOS inverters. It is based on a design provided by Statek Inc, who manufactured the crystal (part number CX-1V-03 171 kHz). The addition of the Schottky diodes, as well as adjustments to the values of the biasing resistors and load capacitors, further improved the duty cycle and insensitivity to fluctuations in the supply voltages. The crystal goes across pads 1 and 2.

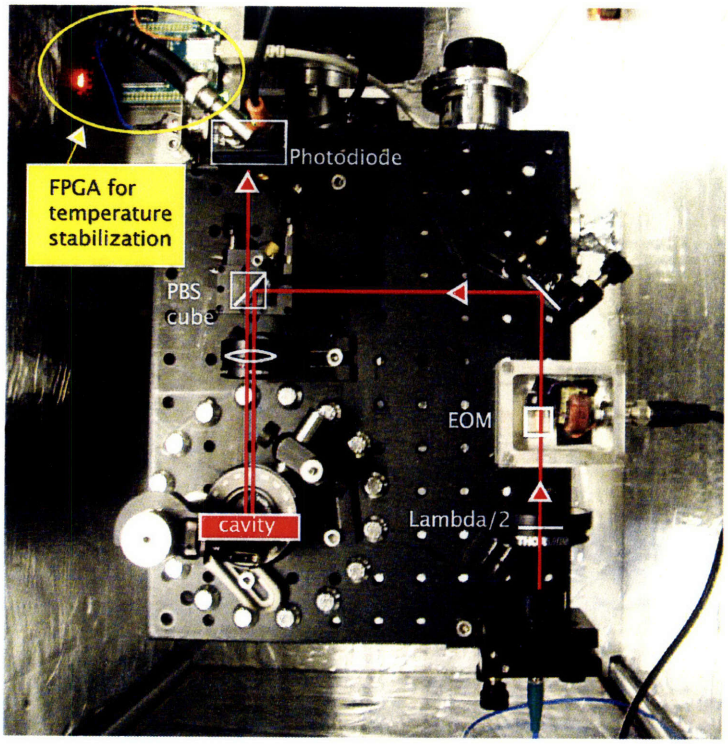

Figure 3-8: A fiber (bottom right) brings a sample of the main beam to the optical cavity (mounted vertically under the optics breadboard, bottom left). The reflected signal is detected by a photodiode (top left). The optical cavity has one flat mirror on the bottom, and another with a radius of curvature of 500mm. The mode-matching lens in between the beamsplitter and cavity has a focal length of 250mm so that the beam is focused on the cavity's flat mirror.

laser phase with an EOM, directing the modulated beam into the etalon, and measuring the reflected signal as shown in figure 3.2.1. Light is delivered to this optics subsystem via a single-mode fiber.

Finally, the entire vacuum enclosure and optics breadboard are placed in a foam-lined box that further insulates the cavity from thermal and acoustic disturbances. It also prevents changes in room lighting from affecting the error signal measurements. The box floats of four legs made of sorbothane, a visco-elastic polymer optimized for vibrational isolation.

3.2.2 Laser frequency detection

The first step of generating the PDH error signal is to modulate the laser beam's phase. An EOM is made from a y-cut KTP crystal[2] that displays a strong Pockels electro-optic effect: the index of refraction varies linearly with applied electric field. The polarization of the incident laser beam is first filtered with a Glann-Taylor polarizer before traveling through the crystal. An amplified 10.24 MHz local oscillator drives a voltage across two copper plates mounted to opposing faces of the crystal, creating a sinusoidal variation in the index of refraction and hence the light's travel time through the EOM.

After the laser beam travels through the EOM and is reflected from the Fabry-Perot cavity, it is incident on a photodiode detector. Section 3.1.2 described how the phase of the cavity's reflection coefficient, and hence the laser frequency's detuning from resonance, is carried by a 10.24 MHz beatnote in the photodiode signal. This beatnote is isolated with a bandpass filter, and then combined with the local oscillator in a mixer. Because the two paths traveled by the local oscillator signal are not the same, a tunable phase shift is introduced between the oscillator and the mixer. Two signals are created at the mixer's output: one at DC and one at $2 \cdot 10.24$ MHz. The DC error signal is isolated with a lowpass filter and then sent to a PI controller which feeds back to the laser, as discussed in the next subsection.

3.2.3 Feedback mechanism

Once the error signal is measured it is fed to an LB1005 PI servo controller made by Precision Photonics of Boulder, CO. The PI controller drives the feedback that cancels frequency fluctuations in the laser. Its output is the sum of two signals: one is Proportional to the magnitude of the error signal and corrects instantaneous errors; the other is proportional to the Integral of past errors, and corrects residual steady-state offsets. The integral controller also speeds up the settling process as control values adjust to slow fluctuations in the laser's frequency.

[2]Ours was manufactured by Casix.

To convert the DC signal at the output of the PI controller into a shift in the laser's frequency, a crystek CVCO55CL-0184-0190 voltage-controlled oscillator (VCO) is used to drive an acousto-optic modulator (AOM). The VCO is an electrical circuit that generates a sine wave at a frequency that can be tuned by a DC input. In our case, the output frequency is centered at 200 MHz and can be shifted 3 MHz/V by the PI controller's output signal.

The VCO/AOM actuator system was chosen because it can be completely external to the existing 674nm laser, which already provides a steady 10 kHz-wide laser beam that is easy to lock to. Direct feedback to the laser's current drive is another popular choice for an actuator in this type of laser lock. Its primary advantage over an AOM is speed – the propagation delay of sound waves in the AOM limits our servo bandwidth to about 1MHz. On the other had, the AOM's response to control inputs is more linear than the response of a laser to its injection current. A third option is to use both an EOM[3] and AOM in series [ZH92]. A high-pass filter sends faster control signals to the EOM, which has a quick response but a narrow tuning range, and a low-pass filter sends the remaining control signal to the AOM, which has a slower response but a much broader tuning range. The main disadvantage of this system is simply the equipment overhead and setup-time required; it may be worth revisiting in the future.

3.3 Summary

The $^{88}Sr^{+}$ optical qubit is extremely sensitive to fluctuations in the frequency of the laser that addresses the $5S_{1/2} \rightarrow 4D_{5/2}$ qubit transition. This chapter has described the theory and design of a new system to stabilize that laser's frequency. We chose to use a Fabry-Perot cavity as a frequency reference, and to lock the laser's frequency to a resonance peak by monitoring the phase of reflected light in the style of a Pound-Drever-Hall lock. The next chapter will characterize this system's performance.

[3]EOMs can be configured as frequency shifters with a careful adjustment of bias voltages that places all of the power into a sideband.

Chapter 4

Characterization of Laser Frequency Lock

In the previous chapter, we saw the theory and design of a new frequency stabilization system for the laser that addresses the optical qubit formed by the $4D_{5/2}$ and $5S_{1/2}$ states of $^{88}Sr^{+}$. The ultimate goal of this system is to improve the precision with which we can manipulate these atomic states, and for this we need an exceptionally stable laser frequency. This chapter describes the diagnostic tools that are used to evaluate the laser lock and provides a characterization of the laser's frequency noise. It begins in section 4.1 with an analysis of the optical cavity as a frequency reference, discussing both the spectral width and time-dependent fluctuations of its resonance. In section 4.2, we turn our attention to the locking mechanism that is responsible for keeping the laser in tune with the cavity resonance.

4.1 The Optical Reference Cavity

A characterization of the optical reference cavity's performance allows us to place limits on the expected performance of the entire PDH frequency stabilization system. In addition, the frequency response of this reference cavity will be necessary to interpret the noise spectrum of the error signal in terms of frequency fluctuations in the laser itself.

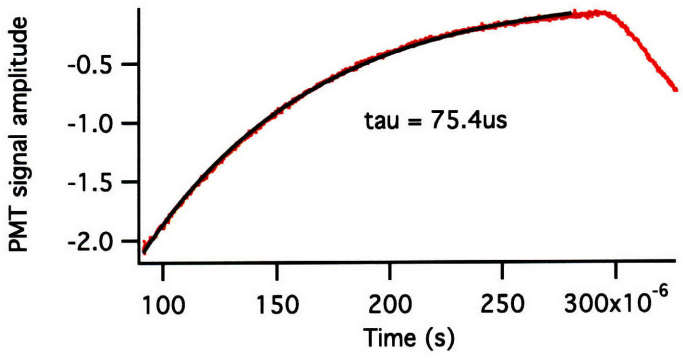

Figure 4-1: The response of the transmitted light signal to a square pulse of resonant light. A more negative amplitude represents a higher power incident on the photomultiplier tube. Shortly before t=100 μs, the laser was turned off, and then turned on again at 300 μs. The power stored in the cavity decayed exponentially with a time constant of 75.4±1 μs after the resonant light was switched off.

4.1.1 Resonance Linewidth and Finesse Measurements

One method of finding an optical cavity's finesse is by measuring the lifetime τ of photons stored between the mirrors, which is related to finesse by the following formula:

$$\mathcal{F} = \frac{2\pi\tau c}{L} \tag{4.1}$$

Here L is 20 cm and c is the speed of light. To measure τ, square pulses of resonant laser light are directed into the optical cavity. During resonant pulses, power builds up to a maximum inside of the cavity. The amount of power that leaks out of the cavity through its mirrors is proportional to this power stored inside. The time-dependent intensity of transmitted light is then measured with a PMT. When the resonant laser light is switched off, the stored power decays exponentially as photons escape the cavity without being replaced by incoming light. This decay reveals the characteristic lifetime of photons in the cavity.

An example measurement of the photon lifetime in the optical reference cavity is shown in figure 4-1. The average of two such measurements indicates a lifetime of $\tau = 75 \pm 1$ μs, which corresponds to a resonance full width at half maximum of $\Delta\nu = 4.24 \pm 0.06$ kHz and a finesse of 708,000±10,000, which is even better than the manufacturer's claims of a finesse between 100,000 and 500,000. The first time that

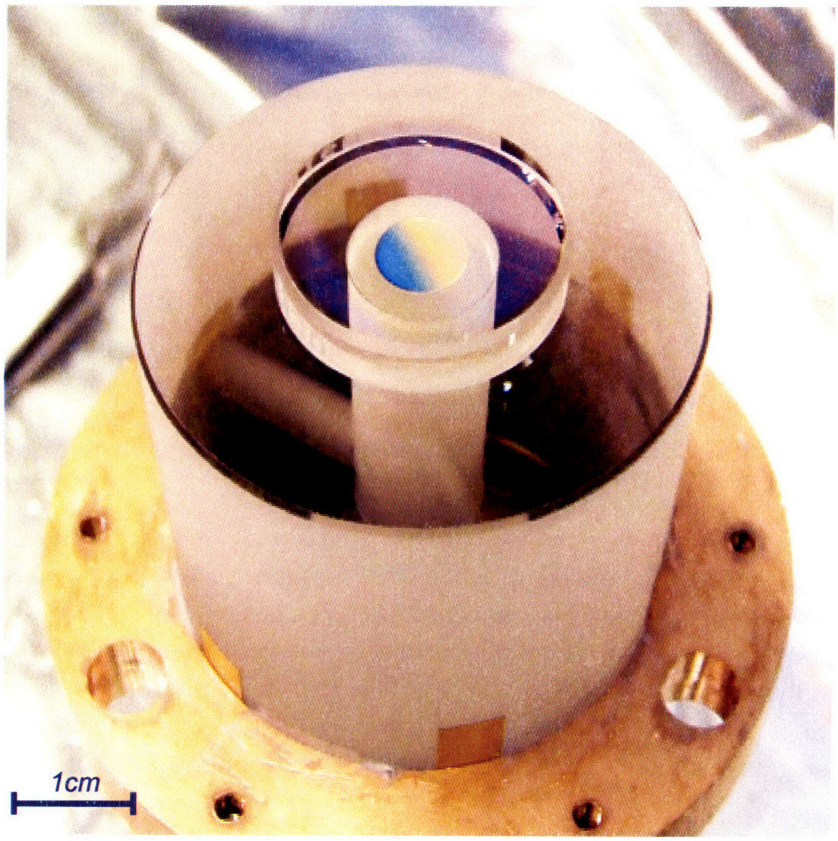

Figure 4-2: The optical reference cavity, with the top half of its copper sheath removed.

cavity ringdown times had been measured, the finesse was found to be only 10,000 and it was returned to have its mirrors cleaned.

The linewidth measurement can also be used to estimate the cavity's gain as a function of[1] frequency f, which will be useful for building a model of the entire locking system. The frequency response of an optical cavity in this arrangement is typically Lorentzian:

$$|H(f)|^2 = \frac{1}{1 + \left(\frac{f}{\Delta\nu/2}\right)^2} \tag{4.2}$$

$|H(f)|^2$ was measured directly by injecting noise into the laser and observing the cavity's response using a lock-in amplifier. The data agrees well with the predicted

[1]There are two different types of frequencies involved in characterizing the lock: the optical frequency distance between the laser and resonance, and the rate at which such frequency fluctuations occur. Here, I refer to the latter.

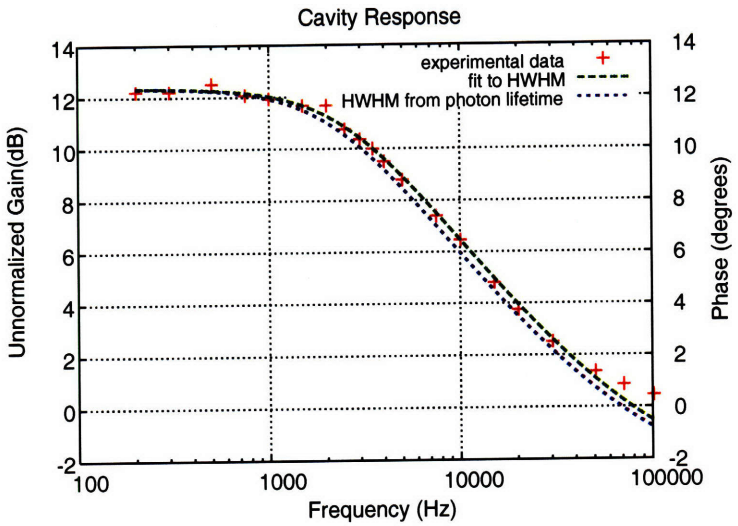

Figure 4-3: The magnitude of the optical cavity's transfer characteristic, as a function of the speed at which the laser's frequency is fluctuating. The Y axis plots $|H(f)|^2$ times an arbitrary constant. The results of the photon lifetime measurement agree well with a direct measurement of the cavity's transfer function, both exhibiting a gain rolloff near 2.1 kHz. This shows that the optical cavity's frequency measurement has the most gain for fluctuations slower than the photon storage time.

$|H(f)|^2$ from the photon lifetime measurement of the cavity's linewidth, which is plotted in figure 4-3.

4.1.2 Stability of the resonance frequency

Recall equation 3.10 from the previous chapter, which shows that fluctuations δL in the mirror separation distance shift the optical cavity's resonance frequency and have an identical effect on the error signal to fluctuations $\delta\omega$ in the laser's frequency:

$$I_{err} \propto \left[\frac{\delta\omega}{\omega} + \frac{\delta L}{L}\right] \tag{4.3}$$

Because the laser lock attempts to drive the error signal to zero regardless of the source of its deviation, instabilities in L are directly projected onto the laser's spectrum. This section will examine the impact of two sources of instability in the optical cavity's resonance frequency: thermal fluctuations and acoustic vibrations.

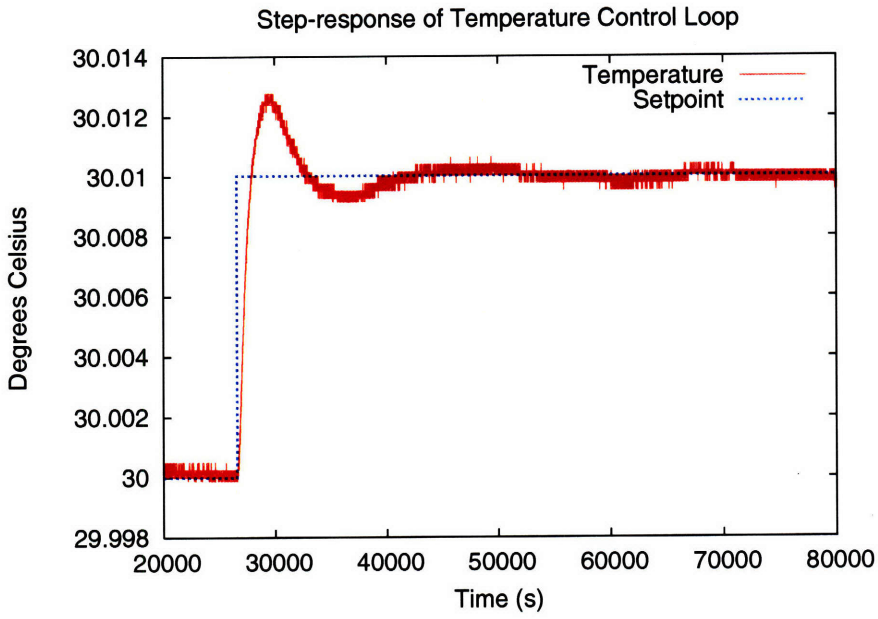

Figure 4-4: Response of the optical cavity's PI temperature controller to a step in the setpoint.

Thermal fluctuations

The expansion coefficient α of ULE glass varies slightly with temperature, but is specified by Corning to lie within $\pm$30ppb/C° at temperatures from 5C° to 35C°. The ULE cavity is typically held at 30C°. Rough measurements of the cavity resonance relative to the Strontium ion's $4D_{5/2} \rightarrow 5S_{1/2}$ indicate that $\alpha \approx$ 7ppb/C°. This means that for a temperature shift of 1mK the mirror spacer's length changes by 0.7pm, which corresponds to a frequency drift of 3 kHz in the cavity resonance.

As described in section 3.2.1 of the previous chapter, the temperature control system consists of a quartz crystal oscillator circuit with a temperature-dependent frequency that is measured by a Field Programmable Gate Array. The FPGA also coordinates the output to a heater wire coiled around the optical cavity mount with a simple PI controller. In the absence of temperature control, the optical cavity system's temperature responds to power from the heater with a time constant of 12 hours. The response of the temperature-controlled system to a step of 0.1 K is shown in figure 4-4. After an initial overshoot of 3mK, the temperature error crosses zero after two hours and settles to a final stability of $\pm$0.6 mK within 19 hours.

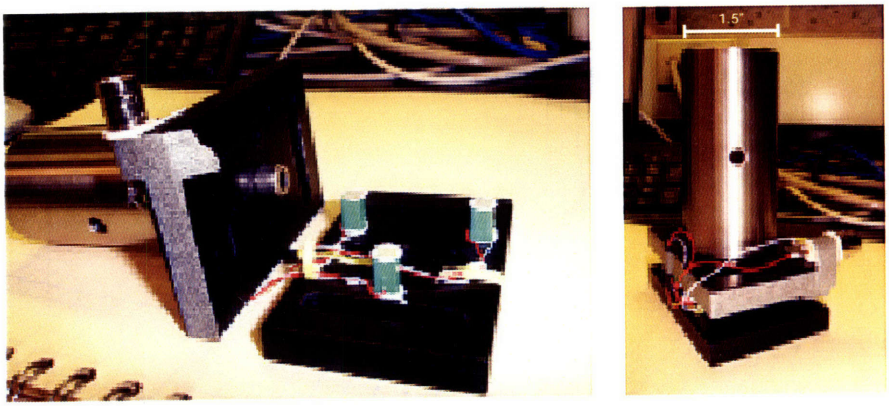

Figure 4-5: A vibration sensor was made by wiring three piezoelectric transducers in series and then fixing them between two optics mounts with torrseal. This configuration allowed the sensor to be rigidly attached to the optics breadboard that directs light into the Fabry-Perot cavity. A wide-base optics post was attached to the top of the sensor so that its weight would increase the sensitivity of the vibration measurement. The AC component of the voltage across the three PZTs was fed to an HPSA 3562A spectrum analyzer.

Although the magnitude of thermal fluctuations in the cavity is potentially problematic, the resulting frequency drifts of the laser are glacially slow in comparison to sub-millisecond timescale on which measurements and quantum gates are executed, and are not a limiting factor in the precision of our experiments.

Acoustic vibrations

The ULE glass has a large Young's modulus of approximately 68 GPa. A force of 1mN between the mirrors shifts the cavity length by about 0.2 pm and mimics a frequency shift of 900 Hz in the laser. This renders the optical cavity's resonance frequency extremely sensitive to vibrations.

To investigate the effect of the laboratory's ambient acoustical noise on the laser's spectrum, a sensor was fashioned from three piezoelectric transducers as shown in figure 4-5. A subwoofer was placed on top of the box that contains the optical cavity's vacuum enclosure, with the speaker directed downwards. The subwoofer was driven at a conversational volume by a signal generator's sine-wave output. To measure the projection of acoustic noise onto the laser spectrum, the output of the PI servo controller to the VCO (see figure 3-4) was measured on a spectrum analyzer.

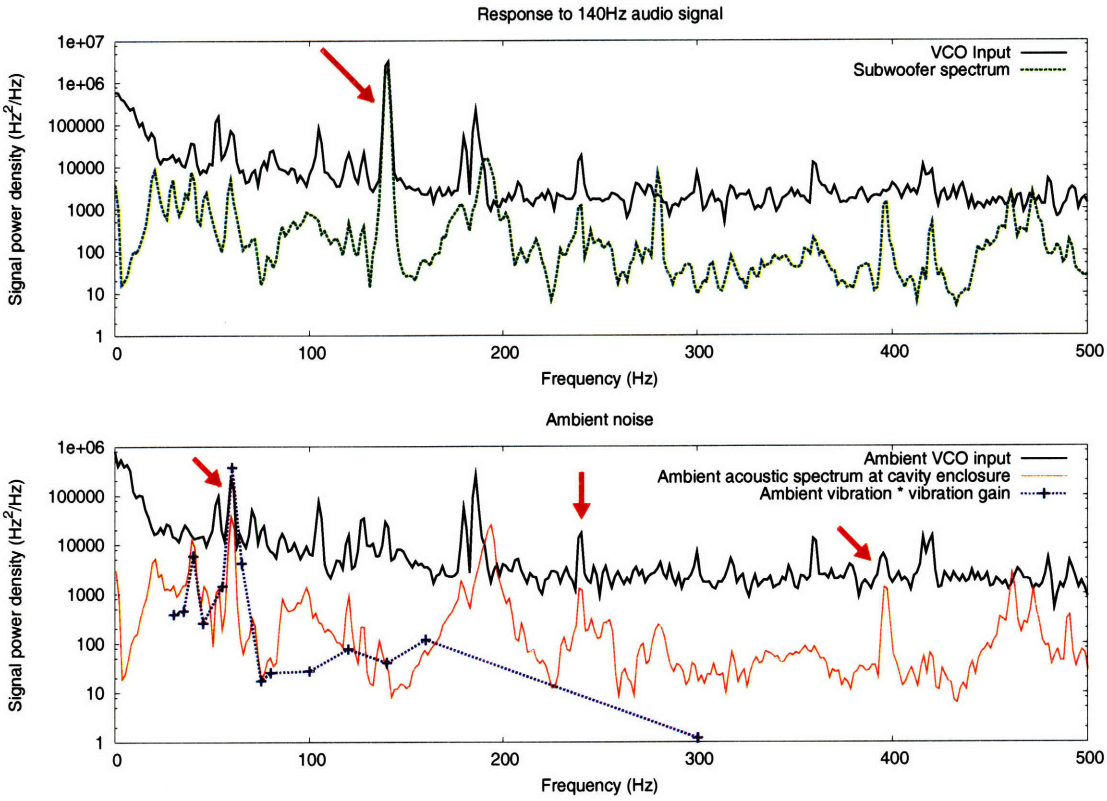

Figure 4-6: Top: the response of a vibration sensor and the control output from the PI controller to the sound of subwoofer tuned to 140 Hz (at a conversational volume). Bottom: Ambient noise spectra in the laboratory. There appears to be a correlation between peaks in the vibration spectrum and peaks in the spectrum of the PI controller signal.

The vibrational spectrum at the optical cavity's vacuum enclosure was measured simultaneously.

A strong correlation was observed between the vibration spectrum and laser control spectrum when the subwoofer was driven at frequencies up to 300 Hz. An example spectrum is shown in the top half of figure 4-6 for a subwoofer frequency of 140 Hz – a corresponding peak at 140 Hz is clearly visible in the servo controller's output to the VCO. The ratio of the spectral powers in this peak of the VCO spectrum to the same peak in the vibration spectrum is plotted as a function of drive frequency in figure 4-7. From this data we can extract a very rough estimate for the gain with which acoustic vibrations are projected onto the laser. Unfortunately, this measurement reveals what is most likely a mechanical resonance in the cavity mount at 63 Hz. In

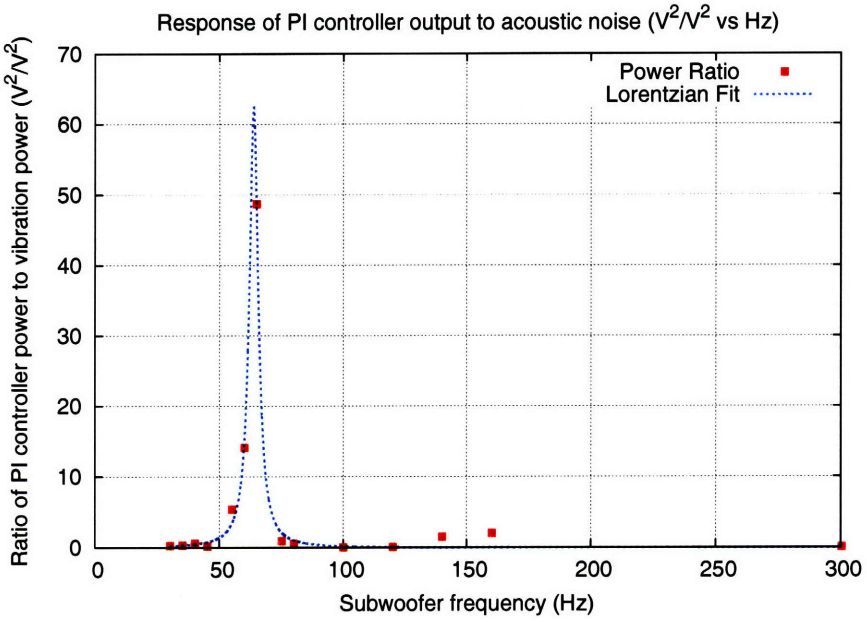

Figure 4-7: Measured response of laser frequency to acoustic vibrations. Each point is extrapolated from a measurement like the one shown in the top plot of figure 4-6. In the measurement, a signal generator drives a speaker to generate acoustic vibrations at a single frequency, which show up as a sharp peak in both the VCO input (PI controller output) spectra and the vibration spectra. The ratio of the magnitudes of the VCO signal and the vibration measurement are plotted. This provides an approximate transfer function to describe the gain with which acoustic noise is projected onto the laser's spectrum.

retrospect, it is clear that the mechanical structure of the cavity mount should have been more carefully modeled ahead of time in order to predict or prevent this resonance, especially because it happens to be so close to the 60 Hz at which laboratory equipment containing electric motors is likely to produce vibrational noise.

The second graph in figure 4-6 shows the ambient vibration spectrum in the lab and the corresponding VCO input spectrum. A third trace combines the ambient vibration data with the gain curve measured in figure 4-7 to estimate the contribution of ambient vibrational noise to the spectrum of the laser. It shows that existing ambient vibrations at a speed of 100's of Hz could cause the lock to pull the laser's frequency by 100's of Hz or even kHz. These frequency fluctuations occur on the timescale of quantum logic operations, and have a significant impact on their fidelity. Chapter 2 discusses how the effects of this noise are mitigated by using spin echoes.

4.2 Lock Performance

So far, this chapter has described the optical reference cavity's performance. Measurements in this section reveal how well the laser's frequency is locked to the cavity resonance, which is used to estimate the laser's spectrum.

4.2.1 The PDH Error Signal

The error signal is important both as the basis for the laser lock and as a mechanism by which we can measure its performance. A theoretical plot of this error signal as a function of frequency was given in figure 3-3. Figure 4-8 shows an experimental measurement of the error signal, which was gathered by sweeping the unlocked laser's frequency rapidly across the resonance.

The most important region of this error signal is the central linear region to which the laser's frequency is locked. The width of this region, which is often called the dynamic capture range, should be roughly equal to the resonance linewidth of 4.24±0.06 kHz. 40 percent of incident laser power is coupled to the cavity when the laser is locked, resulting in a reasonably large amplitude for the error signal. By averaging over many sweeps of the laser across resonance, the height of the error signal was found to be 510 ± 7 mV. Therefore, the sensitivity to fluctuations in laser frequency is $K_{PDH} = \frac{510}{4.24}$ mV/kHz = 0.12±0.01 mV/Hz. This number is important for converting measurements of the error signal into measurements of deviations in the laser's frequency, as described in the next subsection.

4.2.2 Laser noise spectral density, relative to optical cavity

After such painstaking efforts to create a stable and narrow frequency resonance in the Fabry-Perot etalon, we must be sure that the locked laser is indeed tracking its reference. A plot of the loop gain as a function of the rate of frequency fluctuations is shown in figure 4.2.2.

The detection electronics have a bandwidth of approximately 500 kHz. Because gain increases rapidly for decreasing frequencies below the PI corner, the location of

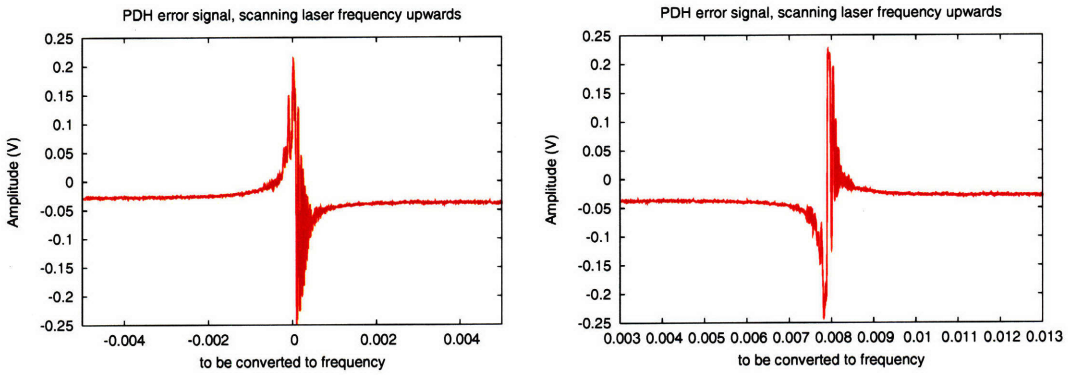

Figure 4-8: The central peak of the PDH error signal, measured by sweeping the unlocked laser's frequency past the cavity resonance. A ringing oscillation occurs after the laser is swept past the resonance in either direction, but this is an artifact of the measurement process and does not reflect an oscillation in the error signal.

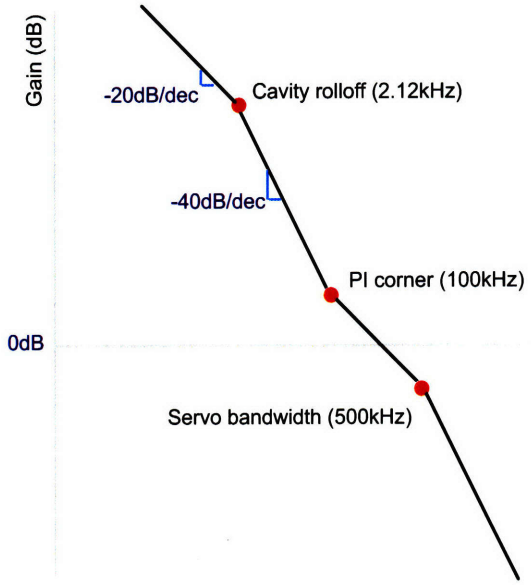

Figure 4-9: A sketch of the frequency response of the lock loop, in dB vs Hz on a log-log scale. The highest gains occur at low frequencies. The transfer funciton of the optical reference cavity in isolation, which rolls off at 2.12 kHz, was discussed in figure 4-3. At frequencies below the PI corner at 100 kHz, the servo controller's integrator contributes a gain with slope of -20 dB/decade. Near 500 kHz, the locking electronics run into speed limitations and there is an RC rolloff that decreases the slope of the transfer function from -20 dB/dec to -40 dB/dec for high frequencies.

this corner was chosen to be 100 kHz. The region between 100 kHz and 500 kHz has a relatively shallow slope of -20 dB/decade. Proportional gain K_P in the PI controller was adjusted to bring the point of 0 dB (unity) gain into this shallow region. Higher gains push the unity gain point beyond the servo bandwidth of 500 kHz, where the phase shift around the loop approaches 180 degrees. This creates positive feedback at higher frequencies and causes oscillations in the lock. Too low a proportional gain would prevent the system from holding the laser's frequency in the linear region of the PDH error signal, making it difficult to lock at all. In order to understand the true impact of K_P, it is useful to calculate an effective gain K_{eff} that includes the constant gains associated with the error signal measurement, which converts frequency shifts to voltages, as well as the VCO, which converts voltages back into laser frequency shifts.

$$K_{eff} = K_p \cdot K_{PDH} \cdot K_{VCO} = 10^{-26dB/10} \cdot \frac{0.00012V}{Hz} \cdot \frac{3 \cdot 10^6 Hz}{V} = 0.9 \qquad (4.4)$$

This represents the DC gain at which frequency corrections are applied to the laser, relative to the size of the error. In the construction of a complete model for the laser lock this number would be particularly useful, however this modeling project was set aside due to time constraints – it was realized that understanding the vibration response of the reference cavity has a much larger impact on the quality of the lock as a whole.

Figure 4-10 shows the power spectral density $S_f(f)$ of the PDH error signal in units of Hz^2/Hz. The error signal is measured at the input to the PI controller (see figure 3-4) with two spectrum analyzers. An HP 3562A measures the $S_f(f)$ for lower frequencies below 100kHz, in terms of mW/Hz. An Agilent E4407B spectrum analyzer measures $S_f(f)$ for higher frequencies, in dBm/Hz, which is then normalized to a measurement bandwidth of 1Hz and converted to mW/Hz. Using the input impedence of 50Ω mW/Hz is converted to V^2/Hz for both signals. Finally, multiplying by $K_{PDH}^2 = (0.12\ \text{Hz/V})^2$, we get the power spectral density in terms of the magnitude of the frequency deviations on the y axis vs. the rate at which they occur on the x

axis.

At low frequencies, the error signal(figure 4-10) has a flat spectral density that is characteristic of white noise. It drops off sharply above 500kHz, the bandwidth of the detection electronics. A purely white signal with constant power spectral density S_f would correspond to a laser with a gaussian frequency spectrum having a linewidth of πS_f. The noise on the laser's error signal has an approximate constant level of 0.1 Hz^2/Hz, so we can estimate a linewidth of 0.31 Hz for the laser's frequency relative to the optical cavity. It is worth strongly emphasizing that this is not the actual linewidth of the laser. Instead, it means that the lock is doing a very good job of driving the error signal to zero for fluctuations slower than 500 kHz – even when shifts in the error signal are not caused by deviations in the laser's frequency. Because electronic noise, thermal fluctuations of the cavity length, and especially acoustic vibrations of the optical cavity mount also affect the error measurement, these noise sources will dominate in the laser's spectrum.

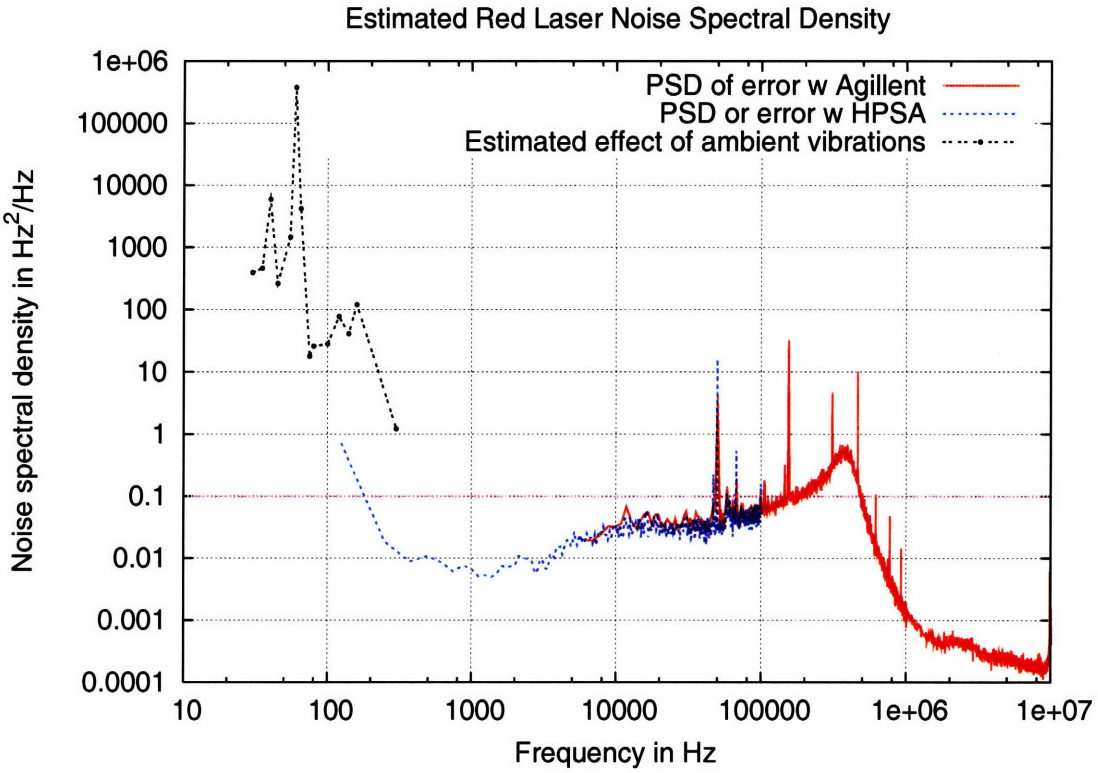

Figure 4-10: The noise spectral density of the error signal, converted into Hz^2/Hz from V^2/Hz using the measured error signal sensitivity value of 0.12±0.01 mV/Hz. A horizontal line is drawn at 0.1 Hz^2/Hz to indicate the white noise level that was used to approximate the locked laser's linewidth. Peaks in the error signal at 50 kHz and 153 kHz are attributed to electronic noise in the lock that controls the original laser before it is stabilized by the PDH system. Data from figure 4-6 is also plotted, showing the expected contribution of acoustic noise to the laser's spectrum.

4.3 Summary

This chapter characterized the laser stabilization system designed in chapter 3. The laser is locked to the resonance of a high-finesse optical cavity to an accuracy on the order of 1 Hz. Noise in the laser's spectrum is therefore dominated by any instabilities in the reference to which it is so tightly locked. Even the smallest change in the separation distance between the mirrors of the optical reference cavity can shift its resonant frequency dramatically – this is because the fractional stability of this distance essentially becomes the fractional stability of the cavity's resonant frequency. A frequency shift by 10 kHz is only four parts in 10^{11} of the resonant frequency of the cavity, and a part in 10^{11} of the mirror separation distance is less than a picometer.

There are two major sources of instability in the mirror separation distance. The first is thermal noise: instabilities in the cavity's temperature cause slow drifts on the order of 10 kHz, but are mostly too slow to affect experiments. In the design process, great care was taken to shield the cavity from thermal gradients and to build a reliable temperature controller, which has allowed this noise to remain as low as it is in magnitude. The second is acoustic vibration, which contributes about 500 Hz to the laser's linewidth on a timescale that is more problematic for experiments. An additional stage of vibration isolation may be needed to further protect the entire cavity mount and vacuum assembly from acoustic noise in the laboratory.

The next two chapters demonstrate the capabilities of the newly stabilized laser by performing coherent manipulations of the ion's quantum states.

Chapter 5

Coherence measurements of the $4D_{5/2} \leftrightarrow 5S_{1/2}$ qubit

When working with quantum systems, it is generally desirable to extend the coherence time as long as possible. So far, this thesis has described the construction of a laser stabilization system designed to reduce the decoherence introduced by classical control. This chapter puts the laser to the test with a series of experiments that were proposed in chapter 2.

In section 5.1, driven coherent oscillations on the carrier transition provide a rough indication of how many consecutive operations could be performed coherently. Section 5.2 uses Ramsey interferometry and spin echo techniques to better understand sources of phase decoherence. In section 5.3, BB1 composite pulses are implemented. The results of these experiments serve to inform our choices of future experiments and to identify potential improvements to the apparatus.

5.1 Rabi oscillations: carrier transition

When the $5S_{1/2} \leftrightarrow 4D_{5/2}$ transition is driven resonantly by a coherent light source, the transition probability oscillates sinusoidally at the Rabi frequency Ω [Rab37]. This frequency indicates the strength with which light is coupled to the atomic resonance as well as the speed at which coherent manipulations of the atom's internal state can

be executed. The theory behind coherent manipulation of atomic states with pulses of light is described more fully in chapter 2.

Fluctuations in the incident laser frequency and power alter the Rabi frequency. These and other sources of decoherence cause a decay in the amplitude of Rabi oscillations with time, limiting the number and fidelity of the coherent manipulations that can be performed on the atom. The Rabi frequency also depends on the ion's motional state $|n\rangle$ (see equation 2.9). Motional heating in our experiments occurs on the time scale of 1 quanta of motion per second [LGA+08], which does not make a large contribution to decoherence on the timescale of this measurement.

Rabi oscillations are measured by scanning the duration of a single resonant laser pulse, as described in chapter 2. Recall the state-space convention introduced in figure 2-1: the full state is given by two qubits $|a, n\rangle$ where $a \in \{0, 1\}$ is the atom's internal state and $n \in \{0, 1, 2, 3...\}$ is its state quantum motion in a harmonic potential. As with all experiments in this chapter, the ion is initially prepared in the $|00\rangle$ by laser cooling. We use the state-dependent florescence signal from the short-lived $S \leftrightarrow P$ cycling transition to measure the atom's internal state. Each data point represents the average of 100 measurements, a process that is described in more detail in chapter 2. Results are plotted in figure 5-1. The data is fit to

$$f(T) = 50 + Ae^{-(\Gamma T)^2/2}\left[\sin^2(\Omega T/2) - 0.5\right] \tag{5.1}$$

where T is the pulse duration. The Rabi oscillations begin with an initial contrast of $A = 98 \pm 1$ % and decay with a time constant of $1/\Gamma = 195 \pm 4$ms. The contrast decays to 80 percent in about 130 μs, enough time for 17 full oscillations. For this particular measurement, the Rabi frequency Ω is 826.7$\pm$0.2 kHz, which means that a single π-pulse has a duration of 3.800$\pm$0.001 μs. This value is an important parameter in the pulse sequences that generate coherent operations. In practice, the Rabi frequency depends on current experimental conditions and must be remeasured at least every few days. Small shifts in the beam alignment and laser power can cause the Rabi frequency to fluctuate by as much as 10 percent over days.

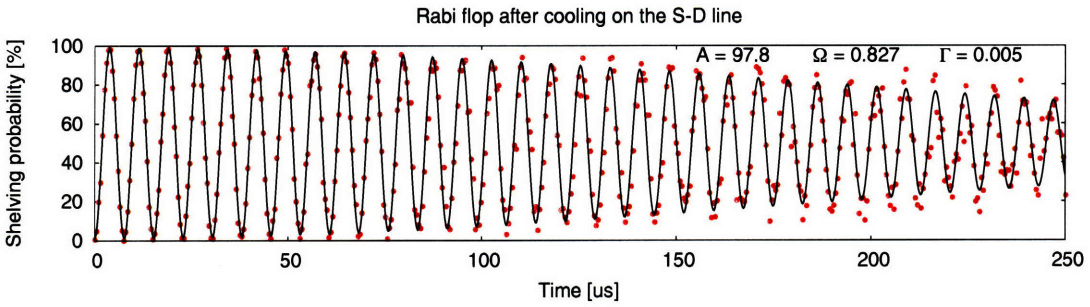

Figure 5-1: Coherent driven oscillations on the $5S_{1/2} \leftrightarrow 4D_{5/2}$ transition.

5.2 Ramsey interferometry

In this section we use Ramsey interferometry [KPRS50] to investigate sources of noise in the ion trapping system, both for the sake of planning future experiments and identifying potential improvements to the apparatus. The atom is first initialized in the $|00\rangle$ state and then subjected to a $\pi/2$-pulse. After a variable period of free evolution, a second $\pi/2$-pulse projects the accumulated phase between the atom and laser onto the z axis of the bloch sphere so that it can be measured via the usual $S \leftrightarrow P$ florescence signal.

A constant detuning of the laser causes the atom's state vector to precess in the laser's rotating frame, generating the famous "Ramsey fringes" – in our case, a sinusoidal oscillation in the amplitude of the florescence signal. Should the detuning of the laser drift over the course of the free evolution period, leading to a mismatch in the $\pi/2$-pulses, the contrast of the Ramsey fringes will be reduced. The noise introduced by a laser having a gaussian spectrum with linewidth Γ would, for example, result in a gaussian envelope on the Ramsey signal with a standard deviation of $T_2^* = 1/(2\pi\Gamma)$. Here, T_2^* can be seen as a conservative lower bound to the experimental coherence time T_2.

The result of the Ramsey measurement is shown in figure 5-2. We see a decay in phase coherence with a gaussian envelope of $T_2^* = 342 \pm 6\ \mu$s which could be caused by, among other things, a laser with broadband gaussian frequency noise and a spectral width of about 465 Hz. However, initial diagnostics of the 674nm laser pointed to a comparatively large spectral component at frequencies below 500 Hz as a dominant

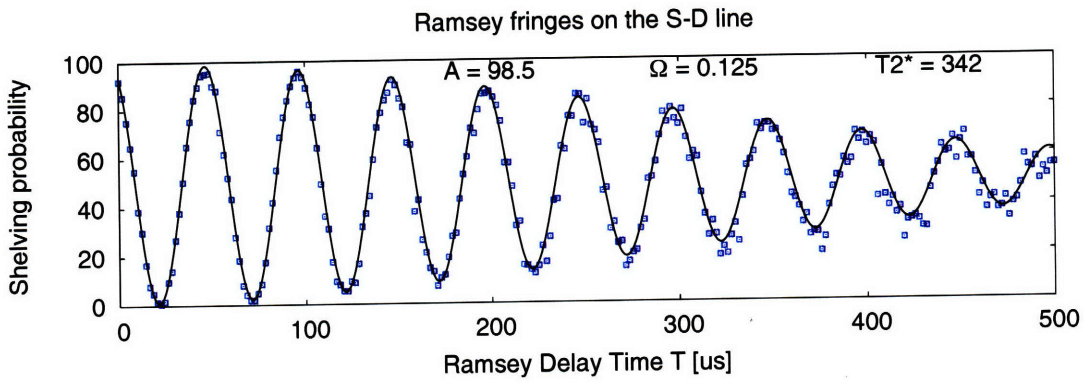

Figure 5-2: The contrast of Ramsey fringes also decays with a gaussian envelope.

noise source. The cases of band-limited noise that only exists at low frequencies vs. broadband noise can be distinguished by spin echo experiments.

5.2.1 Recovery of phase coherence using spin echo

In this experiment, the Ramsey experiment begins with a $\pi/2$-pulse as usual, followed by a period of free evolution with duration τ_0; next, a π-pulse reverses the direction of the atom's state evolution in the laser frame; after a variable time delay τ, the second Ramsey ($\pi/2$) pulse measures the phase between laser and atom. Dephasing that is constant over the time scale of the experiment is effectively cancelled by symmetry when $\tau = \tau_0$ [Hah50].

Figure 5-3 shows the results of several spin-echo measurements for a few values of τ_0. The amplitude of the Ramsey fringes can be recovered to 94±2 % of its original value when τ_0 = 0.5 ms, the length of approximately 100 π-pulses on the carrier transition. This recovered amplitude decays as a function of τ_0, which is plotted in figure 5-5. An inability to recover phases coherence indicates the time scale has become sufficiently long that noise is no longer constant over the course of the experiment. Based on these results the dominant noise appears to be slower than 1 kHz – consistent with the estimated acoustic spectrum in the optical reference cavity that directly measured in section 4.1.2.

In addition to pinpointing specific noise sources, we are interested in understanding

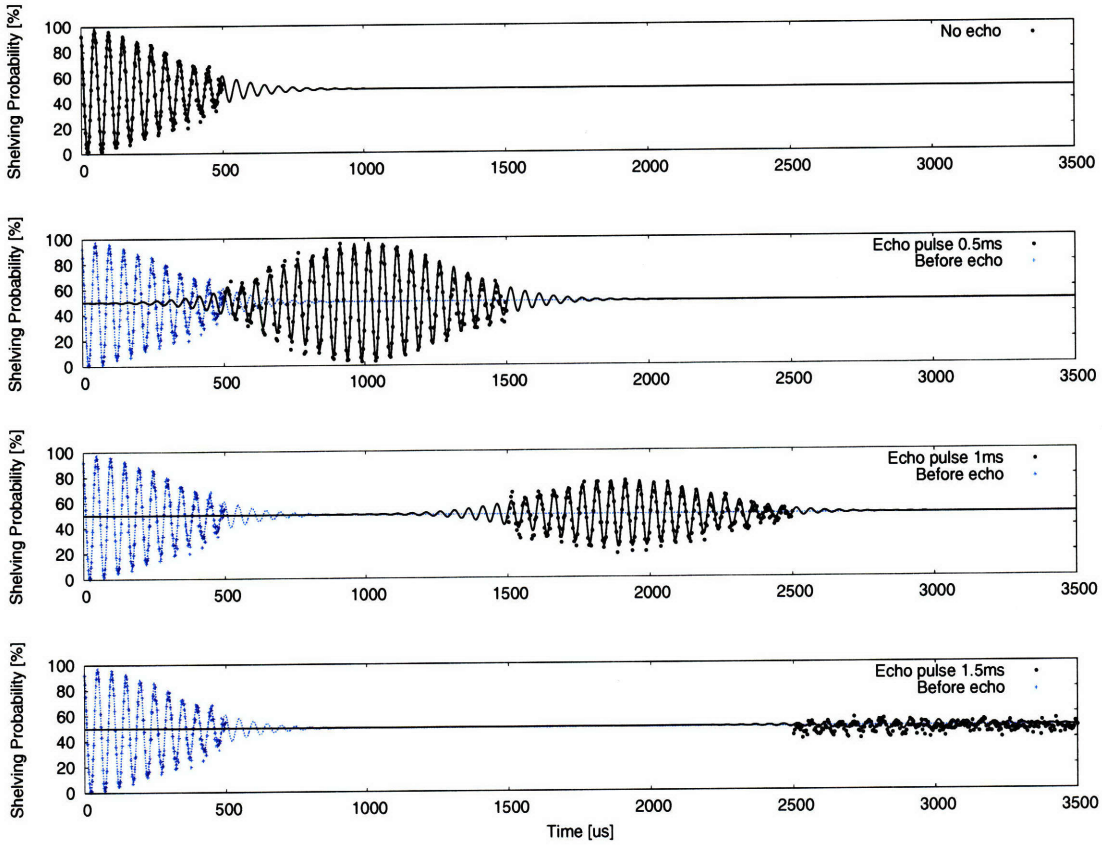

Figure 5-3: Recovery of phase coherence with spin echoes. From top to bottom: 1. The original Ramsey fringes shown in figure 5-2 decay with a time constant of 342±6 μs; 2, 3, and 4 show spin echoes when π-pulses are placed at 0.5 ms, 1 ms, and 1.5 ms respectively. The amplitudes of the echo signals are plotted as a function of time in figure 5-5.

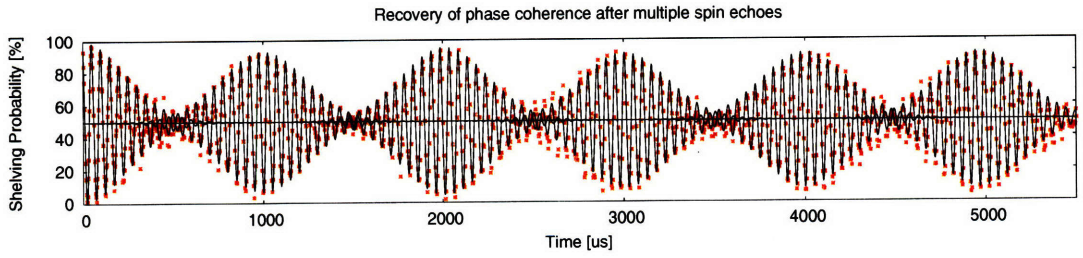

Figure 5-4: The Carr-Purcell sequence, which repeatedly performs spin echoes at regular intervals, places a lower bound of 5 ms on the value of T_2.

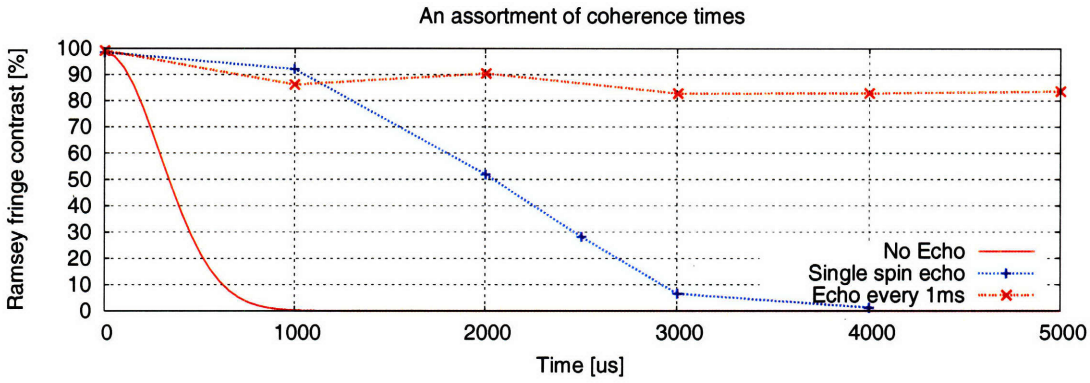

Figure 5-5: Summary of $5S_{1/2} \leftrightarrow 4D_{5/2}$ coherence measurements.

the current limitations of our coherent control of the $^{88}Sr^{+}$ ion. The Carr-Purcell sequence [CP54] is employed to observe the decay of phase coherence that cannot be recovered with spin echo pulses – this decoherence can be mostly attributed to an irreversible loss of information to the surrounding environment. Informed by the results shown in figure 5-3, π-pulses are spaced 1 ms apart at 0.5 ms, 1.5 ms, 2.5 ms, 3.5 ms, 4.5 ms, and 5.5 ms. The decay in the amplitudes of successive echoes reveals that the coherence time T_2 is at least 5ms. Figure 5-5 summarizes the measurements of coherence times made with Ramsey spectroscopy.

5.3 BB1 composite pulses for amplitude errors

BB1 composite pulses, which are described in chapter 2, are widely used in NMR systems to correct for errors in the pulse length T [Wim94]. Fluctuations in the incident laser intensity, for example from fiber noise or unsteady alignment to the atom, would affect θ via Ω in our system. The effect of an error which distorts all rotations by θ into rotations by $\theta[1+\epsilon]$ is reduced to a distortion of $\theta[1+\mathcal{O}(\epsilon^3)]$ in composite BB1 pulses. In this experiment, uniform pulse length errors are deliberately introduced into the BB1 composite pulses designed to perform $R(\pi,0)$ and $R(\frac{\pi}{2},0)$:

$$R_{BB1}(\pi,0) = R(\pi,\phi_1)R(2\pi,3\phi_1)R(\pi,\phi_1)R(\pi,0) \qquad \phi_1 = 82.8^o \tag{5.2}$$

$$R_{BB1}(\frac{\pi}{2},0) = R(\pi,\phi_2)R(2\pi,3\phi_2)R(\pi,\phi_2)R(\frac{\pi}{2},0) \qquad \phi_2 = 75.5^o \tag{5.3}$$

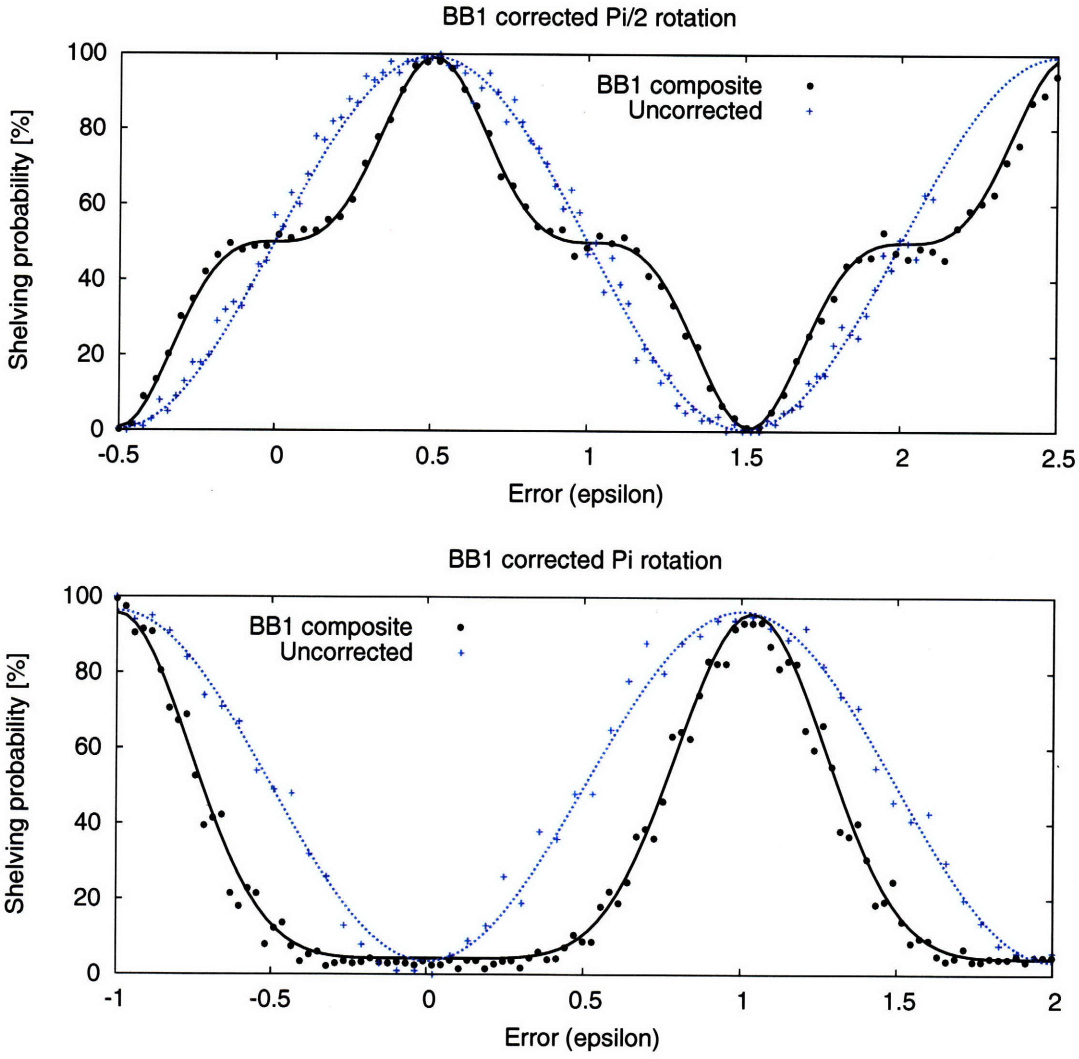

Figure 5-6: Systematic laser amplitude errors and pulse length errors both distort the rotation angle θ to $\theta[1+\epsilon]$. BB1 composite pulses are more resistant to the effects of such errors, as shown by the flat regions near $\epsilon = 0$ for both $\pi/2$- (top) and π-pulses (bottom).

These composite pulses have a longer duration by 4π compared to their uncorrected counterparts, a disadvantage that must often be carefully weighed against the benefits of using composite pulses.

Figure 5-6 shows the result of scanning ϵ for the BB1 composite pulses described above. For a normal uncorrected pulse this action simply generates Rabi oscillations, which are also plotted. The results of these measurements are modeled in Mathematica in the absence of noise, and then fit to two free parameters[1]: the amplitude A and the Rabi frequency Ω. These fits had reduced χ^2 values of 15.2 and 6.7 for the fits to π and $\pi/2$, respectively.

When $\epsilon = 0$, the florescence signal of the BB1-corrected π-pulse shows no improvement in amplitude over the uncorrected version. This result implies that slow fluctuations in the laser's intensity are not a significant source of decoherence on the timescale of these experiments. However, once more significant sources of error are minimized, BB1 pulses could be useful in compensating for systematic pulse length errors caused by an incorrect measurement of the Rabi frequency.

5.4 Summary

Frequency stabilization of the laser has increased the reliability of its coupling to the atomic transition, allowing for coherent Rabi oscillations with an initial contrast of $98 \pm 1\%$ to persist for 17 cycles before the contrast decays to 80%. A measurement of the relative laser-atom phase stability, also greatly improved, was consistent with direct measurements of the magnitude and frequency of vibrational noise in the optical cavity. The amplitude of Ramsey fringes decayed with a time constant of $T_2^* = 342 \pm 6$ μs. After a sequence of five spin echoes spaced 1 ms apart, the Ramsey fringes could be refocused to about 80 % of their original value. Therefore, a conservative lower bound for the coherence time T_2 of the atom's internal state is 5 ms.

In their first published trial with a trapped-ion system, BB1 composite pulses

[1] A is modeled as a constant based on the data in figure 5-1, which shows that the amplitude of Rabi oscillations decays on a time scale much longer than that of a single Rabi flop.

behaved in agreement with theory when systematic pulse length errors were deliberately introduced. They did not otherwise improve fidelity. It can be concluded that systematic laser amplitude noise is not a leading cause of decoherence.

The results in this chapter indicate a high degree of control over the $^{88}Sr^{+}$ optical qubit. In the next chapter, we seek to learn how well this control can be extended to the ion's quantum state of motion.

Chapter 6

Coherent manipulations of $^{88}Sr^{+}$

In the previous chapter we saw that the $^{88}Sr^{+}$ ion's internal state can be controlled with high fidelity, thanks to the laser stabilization system discussed in chapters 3 and 4. Is it possible to extend the use of these tools to a more complex quantum system?To individually address multiple ions in a trap has been done before [SKHR+03], but is beyond our current experimental capabilities. Chapter 2 showed how, by using the ground and first excited states of motion, a single ion could act as a two-qubit system. This chapter describes experimentally the coherent control of both qubits in a $^{88}Sr^{+}$ ion, including the demonstration of a CNOT gate similar to one previously implemented on $^{40}Ca^{+}$ [RLCB+03]. It is, however, the first CNOT to be implemented using a $^{88}Sr^{+}$ ion.

Section 6.1 demonstrates coherent driven Rabi oscillations on the blue sideband, an important signature of quantum control over the motional state. Then, section 6.2 describes the measurement of two-qubit gates, which is used to measure single-pulse rotations on the carrier and sideband transitions. In section 6.3, these pieces are combined to measure a two-qubit gate.

6.1 Rabi oscillations: blue sideband transition

Laser light detuned to the blue sideband drives transitions in the ion's internal and motional states simultaneously, which is the essential first step towards control over

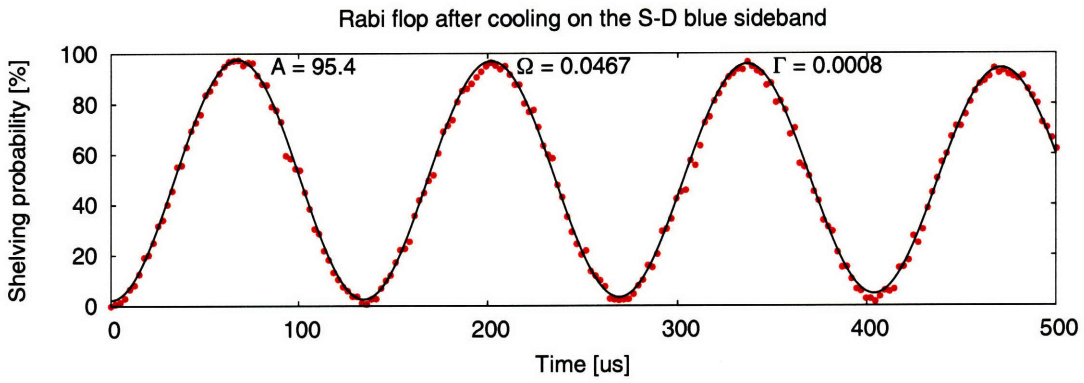

Figure 6-1: Blue sideband Rabi oscillations show coherent control of the ion's quantum motion.

the ion as a two-qubit system. Experimental measurements of coherent driven oscillations on this transition are plotted in figure 6-1 and they look quite promising. The data is fit to

$$f(T) = 50 + Ae^{-(\Gamma T)^2/2}\left[\sin^2(\Omega T/2) - 0.5\right] \tag{6.1}$$

where T is the pulse duration. The oscillations begin with an initial contrast $A = 95.3\pm0.7$ and decay with a time constant of $1/\Gamma = 1.2\pm0.2$ ms. The Rabi frequency Ω is 46.7 ± 0.1 kHz, which means that a single π-pulse has a duration of 66.8 ± 0.2 μs. The possibilities for manipulating the ion's quantum state of motion are therefore more strongly limited by coherence times than they are for the internal electronic state, where the same operation takes only 3.80 ± 0.01 μs.

6.2 Characterization of two-qubit gates

The high contrast of the blue sideband Rabi oscillations indicates a level of coherent control sufficient to realize two-qubit gates on a $^{88}Sr^+$ ion. The other major requirement for building such a gate is a method of characterizing its operation, which in turn requires methods for preparing input states and measuring the resulting ouputs.

State initialization to any of the computational basis states $\{|S0\rangle, |D0\rangle, |S1\rangle, |D1\rangle\}$ is relatively straightforward. An experiment always begins with the ion initialized in the $|S0\rangle$ state. A π-pulse on the carrier or blue sideband brings the ion to the either

$|D0\rangle$ or $|D1\rangle$ respectively. A second π pulse on the carrier can take the ion from $|D1\rangle$ back down to $|S1\rangle$. The initialization of superposition states can be done in a similar fashion.

Measuring the state of the ion after the gate is a much more difficult problem. An ideal measurement would produce an operator that maps every possible input density matrix to the corresponding output density matrix. Unfortunately, there is no mechanism for directly observing the ion's quantum motion – it must instead be mapped onto the electronic state using sideband pulses, which is not a process that can be performed with high fidelity at this stage. Thanks to a clever sequence of pulses devised by Labaziewicz, which I will not describe here [Lab08], it is at least possible to observe the relative populations of the four states after a gate has been performed.

By combining the state initialization and population measurement sequences systematically, one can find the probabilities of transitions between each pair of computational basis states. Arranged into rows and columns according to the states they connect, these measurements form something like a probabilistic truth table. This simplified form of tomography gives only a classical representation of a fundamentally quantum process. Phase is completely neglected. However, it reveals the classical nature of a gate as well as the means to calculate a rough estimate of its fidelity, which we shall call *classical* fidelity. The classical fidelity between two probability distributions $\{p_x\}$ and $\{q_x\}$ is defined by,

$$F(p_x, q_z) = \sum_x \sqrt{p_x q_x}. \tag{6.2}$$

6.2.1 Single-pulse rotations on the carrier transition

The tomography sequence is first tested with an identity (no laser pulse at all) operation as well as π and $\pi/2$ pulses on the carrier transition, because their behavior is already well-understood from the previous chapter. The ideal truth tables for these

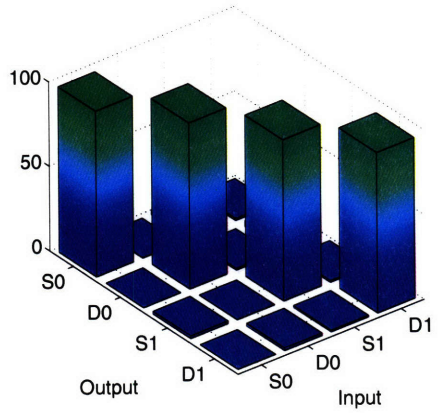

$$\begin{pmatrix} 97.68 & 0.08 & 2.78 & 1.04 \\ 0 & 97.76 & 0.86 & 3.46 \\ 1.48 & 0.04 & 94.94 & 0.88 \\ 0 & 1.46 & 0.84 & 94.50 \end{pmatrix}$$

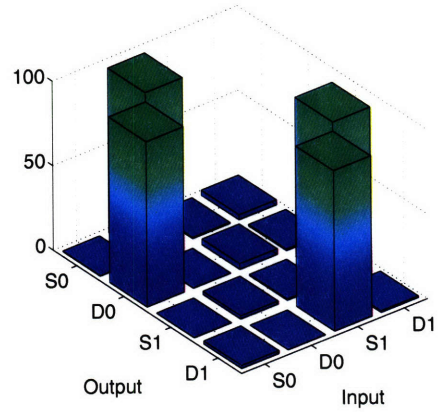

$$\begin{pmatrix} 0.24 & 97.22 & 0.60 & 2.86 \\ 97.64 & 0.02 & 3.24 & 0.78 \\ 0.04 & 1.76 & 0.64 & 94.04 \\ 1.74 & 0.04 & 94.68 & 0.82 \end{pmatrix}$$

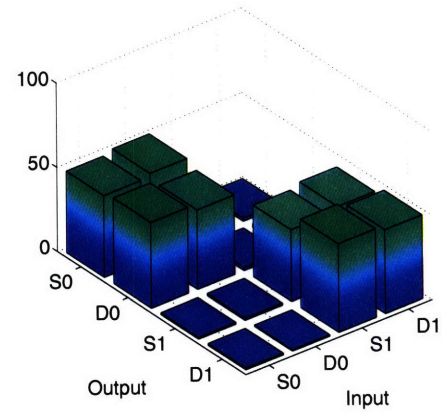

$$\begin{pmatrix} 48.44 & 50.52 & 1.72 & 1.72 \\ 50.72 & 47.08 & 1.68 & 1.86 \\ 0.88 & 1.10 & 42.40 & 45.10 \\ 0.98 & 0.72 & 52.28 & 49.54 \end{pmatrix}$$

Figure 6-2: Input-output truth table measurements for simple carrier pulses: identity, a π-pulse, and a $\pi/2$-pulse (from top to bottom).

three operations are,

$$R(0,0): \begin{pmatrix} 1 & 0 & 0 & 0 \\ 0 & 1 & 0 & 0 \\ 0 & 0 & 1 & 0 \\ 0 & 0 & 0 & 1 \end{pmatrix} \quad R(\pi,0): \begin{pmatrix} 0 & 1 & 0 & 0 \\ 1 & 0 & 0 & 0 \\ 0 & 0 & 0 & 1 \\ 0 & 0 & 1 & 0 \end{pmatrix} \quad R(\frac{\pi}{2},0): \begin{pmatrix} .5 & .5 & 0 & 0 \\ .5 & .5 & 0 & 0 \\ 0 & 0 & .5 & .5 \\ 0 & 0 & .5 & .5 \end{pmatrix} \tag{6.3}$$

where the input states are ordered$\{|S0\rangle, |D0\rangle, |S1\rangle, |D1\rangle\}$ from left to right and the output states follow the same order from top to bottom. The results are plotted in figure 6-2. Each plot represents the average outcome of fifty consecutive identical experiments.

The carrier pulses under test last a small fraction of the time that is required for state initialization and readout sequences. This means that the results in figure 6-2 can be seen as a measure of the classical fidelity of state preparation and readout. The classical fidelities of the identity, π, and $\pi/2$ gates are 0.981, 0.979, and 0.982 respectively. Therefore, the classical fidelity of the measurement and state initialization is 0.981$\pm$0.002.

6.2.2 Single-pulse rotations on the blue sideband

Having so far demonstrated coherent control of the motional state with the Rabi oscillations in figure 6-1, and established a measurement procedure for two-qubit operations, the next logical step is to try a simple operation that acts on both qubits. Figure 6-3 shows the measurement of a π-pulse on the blue sideband. The truth table for this operation is,

$$R^{+}(\pi,0): \begin{pmatrix} 0 & 0 & x & 1 \\ 0 & 1 & x & 0 \\ 0 & 0 & x & 0 \\ 1 & 0 & x & 0 \end{pmatrix} \tag{6.4}$$

The third column is undefined because this pulse couples $|S1\rangle$ to $|D2\rangle$, which is outside of the 2-qubit Hilbert space in which our computations operate. As described

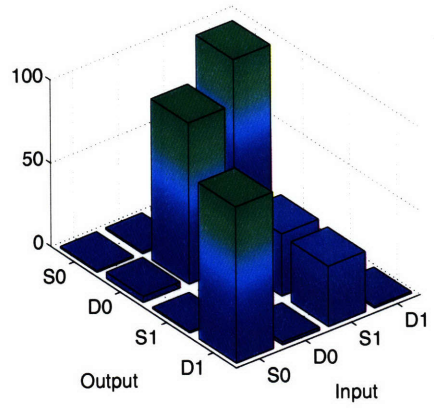

$$\begin{pmatrix} 0.72 & 0.86 & 1.86 & 94.20 \\ 3.52 & 96.32 & 23.78 & 1.10 \\ 0.76 & 0.06 & 37.10 & 2.58 \\ 93.68 & 1.68 & 36.08 & 1.00 \end{pmatrix}$$

Figure 6-3: Truth table of a blue sideband π-pulse. Note that this operation drives a transition from $|01\rangle$ to $|12\rangle$, which is outside of the computational subspace. As with the previous similar measurements, this represents the average of 50 independent trials.

in chapter 2, an important limitation of using the motional state as a qubit is that only certain allowed angles of rotation preserve the computational subspace. For the well-defined transition, the operation performs as expected. The $|S0\rangle \rightarrow |D1\rangle$ and $|D1\rangle \rightarrow |S0\rangle$ transitions are executed correctly and the $|D0\rangle$ is not coupled to any other states as we expect. For these three transitions, the classical fidelity is $0.97 \pm .002$.

One important problem that is not conveyed by figure 6-3 is the systematic phase shift caused by off-resonant AC Stark coupling to the carrier transition during sideband pulses. As described in chapter 2, the offending shift $\phi_{AC} = \delta_{AC} T$ accumulates linearly with the length T of the sideband pulse. By shifting the phases of subsequent pulses by ϕ_{AC} in the opposite direction, the effects of the coupling can be partially cancelled. Ramsey interferometry was used to measure ϕ_{AC} induced by sideband laser pulses as a function of T, as described in [HGR+03]. From these measurements δ_{AC} was measured to be approximately $2\pi \cdot 7$ kHz. Since δ_{AC} depends on experimental conditions such as laser alignment, it must be remeasured at least every time the cryostat is temperature cycled.

6.3 Implementation of a controlled-NOT gate

So far, we have seen coherent control of the ion's internal qubit and motional qubits, as well as the demonstration of an accurate measurement procedure for characterizing a gate. All of the necessary ingredients have been assembled for a CNOT gate. The pulse sequence selected for this experiment is based on one that was previously used by Schmidt-Kaler et al [SKHR+03] to build a CNOT gate between two $^{40}Ca^{+}$ ions, and is explained in chapter 2.

$$U_{CNOT} = R(\frac{\pi}{2}, 2\phi_\pi + 2\phi_{\pi/\sqrt{2}})R^+(\frac{\pi}{\sqrt{2}}, \frac{\pi}{2} + 2\phi_\pi + \phi_{\pi/\sqrt{2}}) \\ \times R^+(\pi, \phi_\pi + \phi_{\pi/\sqrt{2}})R^+(\frac{\pi}{\sqrt{2}}, \frac{\pi}{2} + \phi_\pi)R^+(\pi, 0)R(\frac{\pi}{2}, \pi) \quad (6.5)$$

The phases ϕ_π and $\phi_{\pi/\sqrt{2}}$ are added to compensate for systematic phase errors due to off-resonant coupling to the carrier transition during sideband pulses. The values of ϕ_π and $\phi_{\pi/\sqrt{2}}$ were initially found using the calibration described in section 6.2.2, which occurred immediately before the beginning of the CNOT experiments. We were surprised to find that the fidelity of the CNOT operation appeared consistently higher when the estimated strength δ_{AC} of the stark shift was multiplied by 1.3. The CNOT gate that was measured with this optimized value of δ_{AC} is shown in figure 6-4. This figure represents the average of data from 20 consecutive, identical trials. The classical fidelity of the operation is 0.89±0.02.

It is believed that an incomplete compensation for the effects of off-resonant coupling was a significant source of decoherence in this measurement. Since the data was gathered, a more sophisticated model for the AC Stark shift has been derived [Lab08] that better explains the observed behavior, and may result in even higher fidelities through improved pulse sequences in the future.

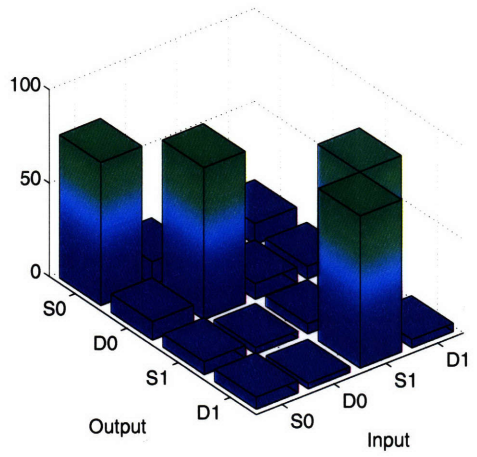

$$\begin{pmatrix} 76.50 & 12.50 & 6.20 & 11.10 \\ 9.81 & 81.25 & 8.25 & 6.70 \\ 6.75 & 3.50 & 5.30 & 75.70 \\ 6.35 & 2.80 & 81.45 & 4.35 \end{pmatrix}$$

Figure 6-4: Truth table measurement of a CNOT gate.

6.4 Summary

This chapter described coherent control of the motional and internal states of a single $^{88}Sr^{+}$ ion. Rabi oscillations on the blue sideband were observed with a period of 133.6±0.4 μs and an initial contrast of 95.3±0.7 percent, indicating that coherent control of the ion's motional state was possible. The characterization of two-qubit gates is complicated by the fact that there is no direct way to observe the ion's motional state. A simplified tomography scheme that measures the transition probabilities between each of the computational basis states was tested on gates constructed from single carrier and sideband pulses. A controlled-NOT gate was then demonstrated with the atom's quantum motion acting as a control bit and the internal state as a target bit. The classical fidelity of this operation was 0.89±0.02.

Chapter 7

Summary and Conclusions

In this thesis, I have described the frequency stabilization of a laser and its application to coherent manipulation of a trapped $^{88}Sr^{+}$ ion. There were two main objectives with these experiments, the first of which was to see how long and by which methods the coherence time of the ion's internal qubit could be extended. In addition to evaluating the purity of the classical control signals carried by the new laser, we had the opportunity to explore methods of recovering from decoherence that take advantage the unique and counterintuitive properties of quantum information. The second goal was to form a two-qubit system from a single ion by coherently controlling the ion's quantum harmonic motion. Such manipulations place stronger requirements on the phase coherence of the atom-laser system than do manipulations of the electronic state. However, they allow immediate access to a richer quantum system and lay some of the ground work for scalable control of multiple ions.

7.1 Laser frequency stabilization

The lifetime of the metastable $4D_{5/2}$ state is on the order of 1 second, which places a very high upper bound on the theoretically acheivable coherence time of the optical $^{88}Sr^{+}$ qubit. The corresponding sub-Hertz natural linewidth of the atomic transition must be addressed by a laser of comparable spectral purity in order for us to begin approaching this coherence time, however. The desire to perform quantum manipu-

lations with high fidelity therefore motivated the construction of a system to stabilize the laser's frequency. A Pound-Drever-Hall scheme was used to lock the laser to the resonant frequency of a high-finesse optical cavity with an accuracy on the order of 1Hz. The lock bandwidth allows frequency drifts that occur as quickly as 500 kHz to be corrected.

In the end though, it is not the tightness of the lock that determines the laser's frequency as much as the stability of the reference it is locked to. The resonant frequency of the optical cavity is highly sensitive to the distance between its mirrors, which are held apart by a ULE glass spacer. A contraction of this distance by even one one-tenth of a Bohr radius shifts the frequency by more than ten kilohertz. Thermal noise causes fluctuations of this magnitude that are mostly too slow to affect experiments. Vibrations in the laboratory at frequencies below 300 Hz were found to propagate to the reference cavity and affect the mirror spacing, introducing a spectral broadening on the order of 500 Hz. This is believed to be a dominant source of technical noise.

7.2 Coherence time of the optical qubit in $^{88}Sr^{+}$

Despite the acoustic noise, the laser stabilization project was quite successful and we find that the ion's internal electronic state can be manipulated by the laser with a high degree of precision. Ramsey inteferometry indicates that phase coherence decays with a time constant of $340\pm6\mu$s. Because the laser's dominant spectral broadening occurs on the slow timescale of acoustic noise, phase coherence can be maintained by spin echoes for over 5ms. This is equivalent to 1000 full Rabi oscillations, ample time for a large number of coherent operations. Future improvements to the acoustic isolation of the optical reference cavity could substantially reduce our dependence on spin echoes for achieving long coherence times.

We also experimented with the use of BB1 composite pulses, which display a reduced sensitivity to systematic errors in the amplitude or duration of control pulses. They are widely used in NMR experiments, but this is the first published use of BB1

on a trapped ion. BB1 composite pulses behaved in agreement with theory when systematic pulse length errors were deliberately introduced. They did not otherwise improve fidelity in our measurements. This implies that our apparatus does not suffer from the types of systematic errors that BB1 pulses are designed to resist. Though it makes for a less interesting demonstration, this comes as a relief to those who would have had to build a lock loop to control the laser's power.

7.3 Manipulations of quantum harmonic motion

Encouraged by the success with coherent manipulations of the atom's internal state, we found it was a natural next step to extend control to a more complex quantum system. Coherent Rabi oscillations on the blue motional sideband of the qubit transition had an initial contrast above 96 percent, indicating a level of coherent control sufficient for treating quantum motion as a second qubit. This level of control was demonstrated more decisively with the implementation of a two-qubit CNOT gate on a single trapped $^{88}Sr^{+}$ ion with a classical fidelity of 0.89 ± 0.02.

Similar experiments traditionally use a second, carefully detuned laser beam to correct for systematic phase shifts caused by off-resonant coupling during sideband pulses. Our implementation instead attempted to compensate for these effects by adjusting phases in the pulse sequences. It was later realized that several approximations made in calculating these shifts resulted in incomplete corrections that could be a limiting factor in gate fidelity. In the future, more precise corrections should allow for higher fidelities in all operations that involve control of the ion's motion, including the CNOT gate.

7.4 Outlook

At this point, the basic building blocks have been assembled for more sophisticated quantum control experiments. The laser stabilization project described in this thesis has brought a high level of precision to our manipulation of quantum information

stored in trapped stronium ions. Measurement of the outcomes of these quantum operations, however, is currently limited to classical probabilities; the implementation of a more complex readout sequence that measures phase would access the fully quantum nature of the system. Many of the most interesting applications of quantum control also involve systems having more than two qubits, where uniquely quantum effects such as entanglement come into play. The controlled-NOT gate demonstrated in this thesis is an important step towards scaling our coherent operations to several ions, because the coupling between internal states and collective motional modes can be used as a form of communication. In the long term, the scaling to quantum control of larger systems has important applications in a variety of scientific pursuits that make use of quantum information techniques, such as the study of quantum-enhanced measurements or even quantum computation.

Bibliography

[AAD+92] Alex Abramovici, William E. Althouse, Ronald W. P. Drever, Yekta Gursel, Seiji Kawamura, Frederick J. Raab, David Shoemaker, Lisa Sievers, Robert E. Spero, Kip S. Thorne, Rochus E. Vogt, Rainer Weiss, Stanley E. Whitcomb, and Michael E. Zucker. LIGO: The Laser Interferometer Gravitational-Wave Observatory. *Science*, **256**(5055), 325–333, 1992.

[BHI+91] J. J. Bollinger, D. J. Heinzen, W. M. Itano, S. L. Gilbert, and D. J. Wineland. A 303-MHz Frequency Standard Based on Trapped Be^+ Ions. *IEEE Trans. Instr. Meas.*, **40**, 126, 1991.

[Bla00] Eric D. Black. An introduction to Pound-Drever-Hall laser frequency stabilization. *Am. J. Phys.*, **69**, 79, 2000.

[BSW82] R. Blatt, H. Schnatz, and G. Werth. Ultrahigh-Resolution Microwave Spectroscopy on Trapped $^{171}Yb^+$ Ions. *Phys. Rev. Lett.*, **48**, 1601, 1982.

[CC01] A. M. Childs and I. L. Chuang. Universal quantum computation with two-level trapped ions. *Phys. Rev. A*, **63**, 012306, 2001.

[CHY+06] Lisheng Chen, John L. Hall, Jun Ye, Tao Yang, Erjun Zang, and Tianchu Li. Vibration-induced elastic deformation of Fabry-Perot cavities. *Phys. Rev. A*, **74**, 053801, 2006.

[CLS+04] J. Chiaverini, D. Leibfried, T. Schaetz, M.D. Barrett, R.B. Blakestad, J. Britton, W.M. Itano, J.D. Jost, E. Knill, C. Langer, R. Ozeri, and D.J. Wineland. Realization of quantum error correction. *Nature*, **432**, 602, 2004.

[CP54] H. Y. Carr and E. M. Purcell. Effects of diffusion on free precession in nuclear magnetic resonance experiments. *Phys. Rev.*, **94**(3), 630–638, May 1954.

[CZ95] J. Cirac and P. Zoller. Quantum computation with cold trapped ions. *Phys. Rev. Lett.*, **74**, 4091–4094, 1995.

[Deu85] D. Deutsch. Quantum theory, the church-turing principle and the universal quantum computer. *Proc. Roy. Soc. London Ser. A*, **400**, 97, 1985.

[DUB+01] S. A. Diddams, Th. Udem, J. C. Bergquist, E. A. Curtis, R. E. Drullinger, L. Hollberg, W. M. Itano, W. D. Lee, C. W. Oates, K. R. Vogel, and D. J. Wineland. An Optical Clock Based on a Single Trapped 199Hg+ Ion. *Science*, **293**, 825, 2001.

[Fey82] R. P. Feynman. Simulating Physics with Computers. *Intl. J. Theor. Phys.*, **21**, 467, 1982.

[For93] Norval Fortson. Possibility of measuring parity nonconservation with a single trapped atomic ion. *Phys. Rev. Lett.*, **70**(16), 2383–2386, Apr 1993.

[Geo08] Elizabeth Marie George. Fiber optic integration in planar ion traps. Bachelor's thesis, Massachusetts Institute of Technology, Physics Department, June 2008.

[Gho95] P. K. Ghosh. *Ion Traps.* Clarendon Press, Oxford, 1995.

[GLM04] Vittorio Giovannetti, Seth Lloyd, and Lorenzo Maccone. Quantum-enhanced measurements: Beating the standard quantum limit. *Science*, **306**, 1330–1336, 2004.

[Hah50] E.L. Hahn. Free nuclear induction. *Phys. Rev.*, **80**, 580, 1950.

[HGR+03] H. Häffner, S. Gulde, M. Riebe, G. Lancaster, C. Becher, J. Eschner, F. Schmidt-Kaler, and R. Blatt. Precision measurement and compensation of optical stark shifts for an ion-trap quantum processor. *Phys. Rev. Lett.*, **90**, 143602, 2003.

[JPD87] R. S. Van Dyck Jr., P. B. Pschwinberg, and H. G. Dehmelt. New high-precision comparison of electron and positron g-factors. *Phys. Rev. Lett.*, **59**, 26, 1987.

[KPRS50] H. G. Kolsky, T. E. Phipps, N. F. Ramsey, and H. B. Silsbee. Radiofrequency spectrum of $d2$ in a magnetic field. *Phys. Rev.*, **80**(3), 483, Nov 1950.

[Lab08] Jaroslaw Labaziewicz. *Scalable Ion Traps for Trapped Ion Quantum Computation.* Ph.D. thesis, Massachusetts Institute of Technology, 2008.

[Lev86] M.H. Levitt. Composite pulses. *Prog. in NMR Spectr.*, **18**, 61, 1986.

[LGA+08] J. Labaziewicz, Y. Ge, P. Antohi, D. Leibrandt, K. R. Brown, and I. L. Chuang. Suppression of heating rates in cryogenic surface-electrode ion traps. *Phys. Rev. Lett.*, **100**, 013001, 2008.

[LGL+08] J. Labaziewicz, Y. Ge, D. Leibrandt, S. X. Wang, R. Shewmon, and I. L. Chuang. Temperature dependence of electric field noise above gold surfaces. 2008.

[LGRS04] V. Letchumanan, P. Gill, E. Riis, and A. G. Sinclair. Optical ramsey spectroscopy of a single trapped $^{88}sr^{+}$ ion. *Phys. Rev. A*, **70**, 033419, 2004.

[LHN+07] A.D. Ludlow, X. Huang, M. Notcutt., T. Zanon-Wileets, S.M. Foreman, M.M. Boyd, S. Blatt, and Jun Ye. Compact, thermal-noise-limited optical cavity for diode laser stabilization at $1x10^{-15}$. *Opt. Lett.*, **32**, 641–643, 2007.

[LRB+07] J. Labaziewicz, P. Richerme, K. R. Brown, I. L. Chuang, and K. Hayasaka. Compact, filtered diode laser system for precision spectroscopy. *Opt. Lett.*, **32**, 572, 2007.

[MBH+04] H. S. Margolis, G. P. Barwood, G. Huang, H. A. Klein, S. N. Lea, K. Szymaniec, and P. Gill. Hertz-Level Measurement of the Optical Clock Frequency in a Single $^{88}Sr^{+}$ Ion. *Science*, **306**, 1355, 2004.

[NC00] M. A. Nielsen and I. L. Chuang. *Quantum Computation and Quantum Information.* Cambridge University Press, Cambridge, UK, 2000.

[NHTD78] W. Neuhauser, M. Hohenstatt, P. Toschek, and H. Dehmelt. Optical-sideband cooling of visible atom cloud confined in parabolic well. *Phys. Rev. Lett.*, **41**, 233, 1978.

[NML+06] Mark Notcutt, Long-Sheng Ma, Andrew D. Ludlow, Seth M. Foreman, Jun Ye, and John L. Hall. Contribution of thermal noise to frequency stability of rigid optical cavity via Hertz-linewidth lasers. *Phys. Rev. A*, **73**, 031084, 2006.

[NMYH05] Mark Notcutt, Long-Sheng Ma, Jun Ye, and John L. Hall. Simple and compact 1-Hz laser system via an improved mounting configuration of a reference cavity. *Opt. Lett.*, **30**, 1815–1817, 2005.

[OBS+07] C.W. Oates, Z.W. Barber, J.E. Stalnaker, C.W. Hoyt, T.M. Fortier, S.A. Diddams, and L. Hollberg. Stable laser system of probing the clock transition at 528nm in nuetral ytterbium. *Frequency Control Symposium, Joint with the 21st European Frequency and Time Forum. IEEE International*, pp. 1274–1277, 2007.

[Pau90] W. Paul. Electromagnetic traps for charged and neutral particles. *Rev. Mod. Phys.*, **62**, 531–540, 1990.

[PS53] W. Paul and H. Steinwedel. Ein neues massenspektrometer ohne magnetfeld. *Z. Naturforsch. A*, **8**, 448, 1953.

[Rab37] I. I. Rabi. Space quantization in a gyrating magnetic field. *Phys. Rev.*, **51**(8), 652–654, Apr 1937.

[RHS+08] T. Rosenband, D. B. Hume, P. O. Schmidt, C. W. Chou, A. Brusch, L. Lorini, W. H. Oskay, R. E. Drullinger, T. M. Fortier, J. E. Stalnaker, S. A. Diddams, W. C. Swann, N. R. Newbury, W. M. Itano, D. J. Wineland, and J. C. Bergquist. Frequency Ratio of Al+ and Hg+ Single-Ion Optical Clocks; Metrology at the 17th Decimal Place. *Science*, **319**, 1808, 2008.

[Ric08] Phillip J. Richerme. Depletion, Quantum Jumps, and Temperature Measruements of $^{88}Sr^{+}$ in a Linear Paul Trap. Bachelor's thesis, Massachusetts Institute of Technology, Physics Department, June 2008.

[RLCB+03] S. Gulde M. Riebe, G. P. T. Lancaster, J. Eschner H. Hffner F. Schmidt-Kaler C. Becher, I. L. Chuang, and Rainer Blatt. Implementation of the Deutsch-Jozsa algorithm on an ion-trap quantum computer. *Nature*, **421**, 48, 2003.

[SKHR+03] F. Schmidt-Kaler, H. Häffner, M. Riebe, S. Gulde, G. P. T. Lancaster, T. Deuschle, C. Becher, Ch. Roos, J. Eschner, and Rainer Blatt. Realization of the Cirac-Zoller controlled-NOT quantum gate. *Nature*, **422**, 408, 2003.

[SNBT86] Th. Sauter, W. Neuhauser, R. Blatt, and P. E. Toschek. Observation of quantum jumps. *Phys. Rev. Lett.*, **57**, 1696, 1986.

[VC05] Lieven M. K. Vandersypen and Isaac L. Chuang. NMR Techniques for Quantum Control and Computation. *Rev. Mod. Phys.*, **76**, 1037, 2005.

[WDW78] D. J. Wineland, R. E. Drullinger, and F. L. Walls. Radiation-pressure cooling of bound resonant absorbers. *Phys. Rev. Lett.*, **40**, 1639, 1978.

[WIBH87] D. J. Wineland, W. M. Itano, J. C. Bergquist, and R. G. Hulet. Laser-cooling limits and single-ion spectroscopy. *Phys. Rev. A*, **36**, 2220, 1987.

[Wim94] S. Wimperis. Broadband, Narrowband, and Passband Composite Pulses for Use in Advanced NMR Experiments. *J. Magn. Reson. B*, **109**, 221, 1994.

[WMI+98] D. J. Wineland, C. Monroe, W. M. Itano, D. Leibfried, B. E. King, and D. M. Meekhof. Experimental issues in coherent quantum-state manipulation of trapped atomic ions. *J. of Res. of the National Inst. of Standards and Technology*, **103**, 259, 1998.

[ZH92] Miao Zhu and John Hall. Stabilization of optical phase/frequency of a laser system: application to a commercial dye laser with an external stabilizer. *J. Opt. Soc. Am. B*, **10**, 802, 1992.

Appendix A

Apparatus for Trapping $^{88}Sr^{+}$

The quantum systems explored in this thesis have been presented in a fairly abstract manner. The purpose of this appendix is to provide some information on how these systems are realized experimentally. Section A.1 describes how an ion trap confines an ion in oscillating electric fields. Section A.2 gives an overview of the experimental apparatus that hosts the ion trap, including the laser system.

A.1 Ion traps

Ions, by virtue of their electric charge, can be confined in electromagnetic potentials. However, to simply create a static three-dimensional potential minimum in free space using an electric or magnetic field alone is forbidden by the laws of classical electrodynamics. One way to circumvent this restriction is to confine ions in time-dependent electric fields that create effective potential minima when averaged over longer time scales. Such traps were developed first by Wolfgang Paul[Pau90, PS53]. Another alternative is to use Penning traps, which combine electric and magnetic fields[JPD87]. All of the data in this thesis was gathered using microfabricated linear quadrupole Paul traps[CLS+04], which closely approximate the potential of the four-rod trap discussed below.

An ion trap can be created from four rod-shaped electrodes arranged in a square pattern as shown in figure A-1. DC voltages on the endcaps of the rods confine the

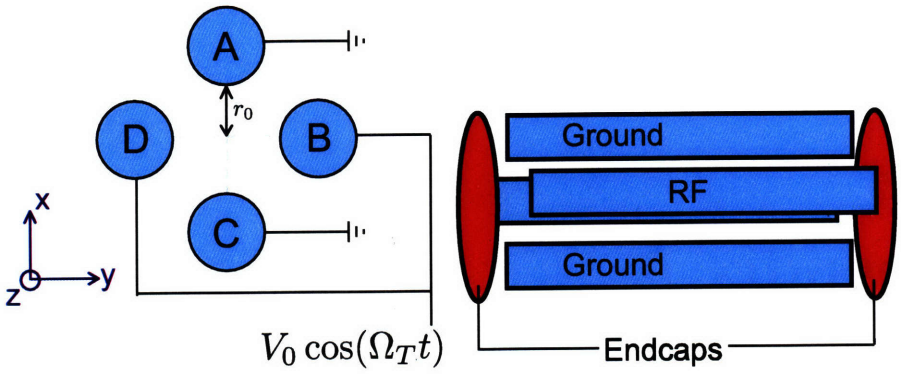

Figure A-1: Left: a cross-section of a four-rod Paul trap. Right: a side view of the same trap, with endcaps shown. A DC bias on the endcaps confines the ion along the axial direction z. Reproduced with permission from [Geo08].

ion in the axial z direction and RF voltages between diagonally opposite rods confine the ion in the $x - y$ plane.

When electrodes A and C are grounded and a voltage V_0 is applied to electrodes B and D, a saddlepoint potential forms in the $x - y$ plane that is perpendicular to the direction of the rods. This potential is approximately hyperbolic:

$$\phi \approx V_0 \left(1 - \frac{x^2 - y^2}{r_0}\right) \tag{A.1}$$

Though the stationary saddlepoint is not a stable confining potential, oscillating voltages on electrodes B and D can generate a time-dependent field that confines the ion to the center of the $x - y$ plane. To see how this works, imagine that just as the ion moved down the saddlepoint potential to escape the trap, you quickly flipped the sign of the voltage on electrodes B and D – the ion now finds itself at a higher potential, and is drawn back to the center of the trap. A continuous rotation of the saddlepoint about the z axis creates an effective potential such that the atom always finds itself at a higher energy when it begins to escape the trap. In this case,

$$\phi \approx \frac{V_0}{2} \cos(\Omega_T t) \left(1 - \frac{x^2 - y^2}{r_0}\right). \tag{A.2}$$

A rigorous analysis of the motion of ions in Paul traps requires the solution of the Mathieu equations[Gho95], which is beyond the scope of this thesis. These are

important for understanding which choices of field strengths, frequencies, and geometric parameters allow for a stable trapping potential. Howevever, a discussion of the secular approximation can still build useful intuition about the system. In the limit that Ω_T is much faster than the ion's motion, an effective harmonic potential is created in the $x-y$ plane. For clarity I will only describe the motion in the x direction, since the solutions are essentially identical for y. The equation of motion for an ion with charge Q is,

$$\ddot{x} = -\frac{QV_0}{mr_0^2}\cos(\Omega_T t)x \tag{A.3}$$

This motion has two components: a relatively slow oscillation in the effective harmonic potential called secular motion (x_{sec}), and a much faster jitter at the drive frequency Ω_T that is called micromotion (x_μ). The total motion is given by $x = x_{sec} + x_\mu$. In the limits of the secular approximation, the micromotion has a much smaller amplitude and much larger frequency than the secular motion.

$$x_\mu \ll x_{sec} \qquad \ddot{x}_\mu \gg \ddot{x}_{sec} \tag{A.4}$$

The motion in equation A.3 then reduces to

$$\ddot{x}_\mu = -\frac{QV_0}{m\Omega^2 r_0^2}\cos(\Omega_T t)x_{sec} \tag{A.5}$$

and we can also find that

$$x_\mu = \frac{QV_0}{mr_0^2\Omega_T^2}\cos(\Omega_T t)x_{sec} \tag{A.6}$$

Plugging these last two equations back into equation A.3, we have

$$\ddot{x}_{sec} = -\frac{Q^2V_0^2}{m^2r_0^4\Omega_T^2}\cos^2(\Omega_T t)x_{sec} \tag{A.7}$$

$$\ddot{x}_{sec} = -\frac{Q^2V_0^2}{2m^2r_0^4\Omega_T^2}x_{sec} \equiv -\omega_x^2 x_{sec} \tag{A.8}$$

where we have assumed that the $\cos^2(\Omega_T)$ is fast enough to average out to $\frac{1}{2}$ on the time scale of the slow secular motion in the harmonic potential, which has a frequency of ω_x.

To summarize the linear quadrupole trap, ions are confined in the axial direction by DC voltages on the endcaps. In the radial directions, the ions are more tightly confined by the oscillating RF potential between the rods. The result is a cigar-shaped effective confinement potential that can trap a long chain of ions. This potential is approximately harmonic, with radial oscillator frequencies of $\omega_x = \omega_y = \sqrt{\frac{QV_0}{2mr+0^2\Omega_T}}$.

A.2 The ion trapping system

This section presents an overview of the experimental apparatus that is used to trap ions. The goal of this system is to isolate an ion as well as possible from interactions with its surrounding environment, while still allowing optical access for measurement and interaction with lasers. I present only enough details here to understand the data in chapters 5 and 6; the authoritative reference on this system's design and operation is the PhD thesis of Labaziewicz[Lab08].

A.2.1 Cryogenic vacuum environment

Because collisions with background gas disrupt the trapping process, the chamber containing the ion trap is held at a pressure better than 10^{-10} Torr. Such vacuum levels are more easily achieved at cryogenic temperatures, where activated charcoal getters can pump out residual gas and the suppression of outgassing allows for materials that are not typically considered vacuum-friendly. Interestingly, it has also been found that decoherence of the ion's motional state is dramatically reduced at low temperatures[LGA+08]. This effect appears to be related to fluctuations in the electric field on the metal surface of the ion trap[LGL+08].

The trap is operated inside of a bath cryostat. It is fixed to a baseplate that is held at 4K by a tank of liquid helium, as shown in figure A-2. A 77K thermal shield, cooled by a tank of liquid nitrogen, surrounds the helium bath and trapping region.

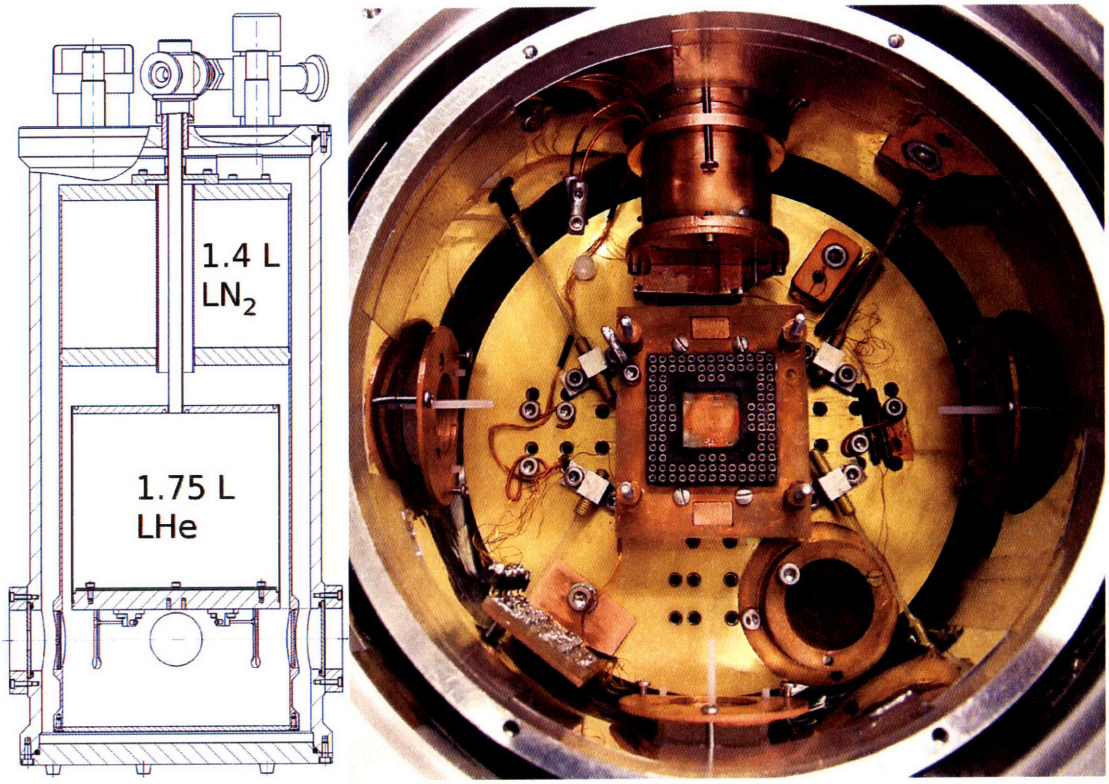

Figure A-2: Left: a schematic of the cryostat. Right: a view of the inside of the cryostat, looking from the bottom up. The trap is mounted to the square CPGA socket in the center. Optical viewports for lasers are located at the left, right, and bottom edges of the picture. At the top of the picture is the RF resonator (in the copper cylinder) that drives the trap potential. Reproduced with permission from [Lab08].

Windows in the sides and bottom of the vacuum shield allow optical access to the surface of the trap. The entire vacuum enclose is pumped with a turbo pump.

Due to the Zeeman effect, the energy splitting between the $4D_{5/2}$ and $5S_{1/2}$ qubit states has a first-order sensitivity to fluctuations in magnetic field strength – this is often an important source of decoherence. The magnetic field is first biased using Helmholtz coils wound around the outside of the cyrostat. Superconducting niobium rings are also placed above and below the ion trap. This geometry utilizes the tendency of superconductors to resist changes in magnetic flux, and provides a high degree of magnetic field stabilization.

Strontium ions are also produced inside of the cryostat. First, a resistive oven ejects nuetral atoms from a piece of strontium metal. The nuetrals are then photoionized in a two stage process by laser light at 460nm and 405nm. Once charged, the ions can be trapped.

A.2.2 Optics and laser system

Light is our primary method of interacting with the ion. Lasers at six different frequencies must be aligned to the trap through the cryostat's side windows in order to produce, control, and observe an ion. A light collection system, used to detect the ion's florescence signal, is located on the other side of a window in the bottom of the cryostat.

Ion imaging and scatter detection

The 422nm light scattered by the ion's $S-P$ transition is used both for state detection and imaging of trapped ions. Scattered light is first collumnated with a 24mm aspheric lens located near the trap. Outside of the cryostat, the light is passed through a 422nm notch filter and a 70/30 beamsplitter. The stronger beam is focused on a photomultiplier tube, which uses the strength of the florescence signal to measure the ion's quantum state in the shelving scheme that was described in section 2.4.1. A CCD camera measures the weaker beam. Before trapping, this camera is used to

view the trap and simplify the alignment of lasers. While loading the trap, it is used to measure the position and number of trapped ions.

Monolithic laser system

Four lasers are used to control the atomic transitions of $^{88}Sr^{+}$: 422nm for cooling and readout, 1033nm and 1092nm for repumping, and 674nm to address the optical qubit. The fact that all of these wavelengths can be generated by commercially available semiconductor laser diodes was part of the reason that the $^{88}Sr^{+}$ ion was chosen for our experiments. Laser diodes are reliable, compact, and often cheap. However, with a typical linewidth of 1MHz they do not possess the level of spectral purity that is required for coherent control.

A monolithic laser system built around these laser diodes narrows the output linewidth to 10kHz[LRB+07], shown in figure A-3. Each diode is installed in an Extended Cavity Diode Laser configuration, with an external medium-finesse filter cavity used to remove background florescence and stabilize the laser frequency. The diode, ECDL, and cavity are mounted on a temperature-stabilized aluminum base-plate inside of an evacuated box. Each of these laser systems is referred to as a monolaser.

The monolithic 674nm qubit laser is able to cool the ion to the ground state of its motion and drive coherent Rabi oscillations on the $4D_{5/2} \leftrightarrow 5S_{1/2}$ transition. However, further stabilization is required before more advanced quantum control is possible. The theory and design of a secondary frequency stabilization system, which uses a high-finesse optical cavity as a reference, is presented in chapter 3.

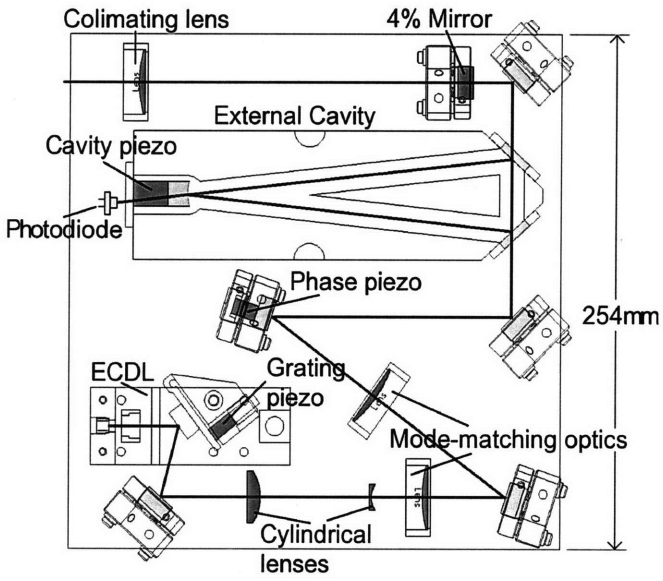

Figure A-3: A schematic of a monolithic laser setup, with a superimposed laser beam. Reproduced with permission from [LRB+07]. A digital feedback system controls the phase and piezo gratings based on the signal at the photodiode in the external filter cavity.